Monthly Notices of the ROYAL ASTRONOMICAL SOCIETY

MNRAS **530,** 4474–4492 (2024) https://doi.org/10.1093/mnras/stae1116
Advance Access publication 2024 April 24

MaNGA DynPop – V. The dark-matter fraction versus stellar velocity dispersion relation and stellar initial mass function variations in galaxies: dynamical models and full spectrum fitting of integral-field spectroscopy

Shengdong Lu [1]★ Kai Zhu [2,3,4] Michele Cappellari [5] Ran Li [2,3,4] Shude Mao [1] and Dandan Xu[1]

[1]*Department of Astronomy, Tsinghua University, Beijing 100084, China*
[2]*National Astronomical Observatories, Chinese Academy of Sciences, 20A Datun Road, Chaoyang District, Beijing 100101, China*
[3]*Institute for Frontiers in Astronomy and Astrophysics, Beijing Normal University, Beijing 102206, China*
[4]*School of Astronomy and Space Science, University of Chinese Academy of Sciences, Beijing 100049, China*
[5]*Sub-department of Astrophysics, Department of Physics, University of Oxford, Denys Wilkinson Building, Keble Road, Oxford OX1 3RH, UK*

Accepted 2024 April 22. Received 2024 April 11; in original form 2023 September 21

ABSTRACT

Using the final Mapping Nearby Galaxies at Apache Point Observatory sample of 10K galaxies, we investigate the dark matter (DM) fraction $f_{\rm DM}$ within one half-light radius $R_{\rm e}$ for about 6K galaxies with good kinematics spanning a wide range of morphologies and stellar velocity dispersion. We employ two techniques to estimate $f_{\rm DM}$: (i) Jeans anisotropic modelling (JAM), which performs DM decomposition based on stellar kinematics and (ii) comparing the total dynamical mass-to-light ratios $(M/L)_{\rm JAM}$ and $(M_*/L)_{\rm SPS}$ from stellar population synthesis (SPS). We find that both methods consistently show a significant trend of increasing $f_{\rm DM}$ with decreasing $\sigma_{\rm e}$ and low $f_{\rm DM}$ at larger $\sigma_{\rm e}$. For 235 early-type galaxies with the best models, we explore the variation of stellar initial mass function (IMF) by comparing the stellar mass-to-light ratios from JAM and SPS. We confirm that the stellar mass excess factor $\alpha_{\rm IMF}$ increases with $\sigma_{\rm e}$, consistent with previous studies that reported a transition from Chabrier-like to Salpeter IMF among galaxies. We show that the $\alpha_{\rm IMF}$ trend cannot be driven by M_*/L or IMF gradients as it persists when allowing for radial gradients in our model. We find no evidence for the total M/L increasing toward the centre. We detect weak positive correlations between $\alpha_{\rm IMF}$ and age, but no correlations with metallicity. We stack galaxy spectra according to their $\alpha_{\rm IMF}$ to search for differences in IMF-sensitive spectral features (e.g. the $\rm Na_I$ doublet). We only find marginal evidence for such differences, which casts doubt on the validity of one or both methods to measure the IMF.

Key words: galaxies: stellar content – galaxies: evolution – galaxies: formation – galaxies: fundamental parameters – galaxies: kinematics and dynamics.

1 INTRODUCTION

Stellar mass of galaxies is a key property which encodes the information of galaxy formation and evolution. By comparing the stars initially formed and those present-day observed, we are able to constrain the detailed evolution tracks of the galaxies. Thus, the stellar initial mass function (IMF), which describes the number distribution of newly formed stars of different masses, is a crucial factor to reveal the stellar mass assembly history of the galaxies. The first attempt to describe the IMF is Salpeter (1955), which proposed a single power law (PL) of the number distribution of newly formed stars of different masses at birth, i.e. $\phi \propto m^{-2.35}$. Later on, Kroupa (2001) and Chabrier (2003) reported a flatter slope at low-mass end (i.e. lower than 0.5 $\rm M_\odot$) of the IMF for the Milky Way (MW).

To study the IMF of the MW, one can make use of direct stellar counting (e.g. Kroupa, Tout & Gilmore 1993; Phelps & Janes 1993; Reid & Gizis 1997; Carraro et al. 2005; Bonatto & Bica 2007). Kroupa et al. (1993) analyzed the luminosity functions of a sample of stars within 5.2 pc of the sun and a magnitude-limited sample of more distant stars and concluded that the two samples can be described by a single broken PL IMF, which becomes the basis of the Kroupa (2001) IMF. Phelps & Janes (1993) summarized the studies on MW IMF with open clusters and found that most open clusters agree with the Salpeter IMF at the mass range of 1−8 $\rm M_\odot$. At the sub-solar mass range, Moraux et al. (2003) studied the IMF slope down to 0.03 $\rm M_\odot$ with the Pleaides and found that a lognormal form can well describe the IMF over a broad mass range (0.03−10 $\rm M_\odot$). Combining a large number of literature, Bastian, Covey & Meyer (2010) claimed in their review that there was little compelling evidence for variations in the IMF across different galaxies or within our own about 10 years ago. More recently, Li et al. (2023) pointed out that the IMF inside the MW varies with metallicity and cosmic time, by counting 93 000 spectroscopically observed M-dwarf stars in the solar neighbourhood. So far, whether the IMF of MW varies is still an important question to address.

For external galaxies, however, one can hardly resolve single stars, and thus, cannot estimate the IMF from direct stellar counts as done

★ E-mail: lushengdong93@icloud.com

in the MW. There are two main methods to study the IMF of external galaxies. One is the spectroscopic approach, which makes use of the IMF-related spectral features or the full spectrum to constrain the IMF shape of galaxies. The other is to compare the stellar mass (or stellar mass-to-light ratio) derived in a luminosity-independent (and hence, IMF-independent) way and that derived with stellar population synthesis (SPS), assuming a standard IMF. The luminosity-independent stellar mass (stellar mass-to-light ratio) can be obtained either by stellar dynamical modelling or by gravitational lensing.

Earlier studies used the spectral features to point out that either the IMF or the chemical abundance may be different among galaxies, but they could not distinguish between the two effects (e.g. Faber & French 1980; Carter, Visvanathan & Pickles 1986; Cenarro et al. 2003). Similarly, initial studies using galaxy dynamics (Cappellari et al. 2006) or gravitational lensing (Treu et al. 2010) noted that the central M/L variations among galaxies could not all be attributed to variations of the stellar population M/L alone, but could not distinguish between the effects of dark matter (DM) or the IMF. Two independent studies first made a convincing case for a heavier-than-MW IMF using either strong lensing (Auger et al. 2010) or spectral features (van Dokkum & Conroy 2010). The latter showed the IMF, and not chemical abundance, was responsible for the observed spectra variations. They reported that the gravity-sensitive spectral features (i.e. the Na_I doublet and the Wing–Ford molecular FeH band) can be detected in the spectra of the most massive elliptical galaxies, indicating the high richness of dwarf stars and hence pointing out the IMF is more bottom-heavy than Salpeter in those massive elliptical galaxies (i.e. steeper slope at $m < 0.3\,M_\odot$).

Using the galaxy–dynamics approach, Cappellari et al. (2012) made use of the Jeans anisotropic modelling (JAM; Cappellari 2008, 2020) to get the luminosity-independent stellar mass-to-light ratio of 260 early-type galaxies (ETGs) from the ATLAS^{3D} survey (Cappellari et al. 2011) and concluded that the previously reported Salpeter-like IMF in massive galaxies was just the extreme of a systematic trend with the stellar IMF being Chabrier-like for low-mass ETGs and becoming heavier with increasing stellar mass-to-light ratio or velocity dispersion of galaxies. More details of the effort were given in Cappellari et al. (2013b), who also showed that the IMF correlated better with velocity dispersion than with the mass or size of galaxies.

Following the initial reports, several subsequent studies corroborated the findings, generally supporting the original outcomes. Spiniello et al. (2012), Spiniello, Trager & Koopmans (2015), Conroy & van Dokkum (2012), and van Dokkum & Conroy (2012) reported a trend between IMF and stellar velocity dispersion using the spectral features approach. La Barbera et al. (2013) used spectral features to study the IMF variation against velocity dispersion of galaxies with 24 781 ETGs from the SPIDER sample (La Barbera et al. 2010) and found that IMF varies from a Kroupa/Chabrier case towards a more bottom-heavy IMF with increasing central velocity dispersion. Zhou et al. (2019) adopted a full spectrum analysis on the IMF variation among galaxies from the Mapping Nearby Galaxies at Apache Point Observatory (MaNGA) survey (Bundy et al. 2015) and found the similar IMF trend with velocity dispersion. Other IMF-relevant studies with the spectroscopic approach include Ferreras et al. (2013), Martín-Navarro et al. (2015a, b), van Dokkum et al. (2017), Parikh et al. (2018), and Gu et al. (2022). Dutton et al. (2013) studied the IMF in the bulges of massive spiral galaxies by comparing the stellar mass-to-light ratio from strong lensing and gas kinematics, and that from SPS. Other studies on IMF variation with such method include Thomas et al. (2011), Li et al. (2017), Shetty et al. (2020), and Loubser et al. (2021). The readers are referred to Cappellari (2016, section 4.2.2) for a summary of the earlier IMF results and to Smith (2020) for a more extended review of the IMF variation among external galaxies.

Although both the spectroscopic method and the dynamical/lensing method agree with each other on the IMF variation with velocity dispersion of galaxies, there are conflicts between the two methods. Conroy & van Dokkum (2012) found that the IMF becomes more bottom-heavy with increasing [Mg/Fe] (similar results also see Gu et al. 2022), although La Barbera, Ferreras & Vazdekis (2015) claimed that this correlation is driven by the IMF-dispersion relation and no extra correlation between IMF and [Mg/Fe] has been seen with the similar method. Zhou et al. (2019), with a full spectrum analysis, also found similar trend of IMF shape against total metallicity (i.e. $[Z/H]$) of galaxies. However, with a dynamical modelling-based method, Thomas et al. (2011) and McDermid et al. (2014) found no obvious relation between IMF and metallicity of galaxies. Smith (2014) made a detailed comparison of the IMF shape constrained by dynamical modelling-based method and the spectroscopic method on the same galaxy sample. They found that although both methods recover the IMF-velocity dispersion trend, there is no correlation between the stellar mass excess factor inferred from the two approaches on a galaxy-by-galaxy basis. They commented that one (or both) of the methods may have not accounted fully for the main confounding factors of IMF variation and suggested that a comparison between the IMF constrained with the two methods in the same aperture would be necessary to further understand the difference.

With a series of papers of the MaNGA DynPop (dynamics and stellar population) project, we aim to not only provide catalogues containing the dynamical and stellar population properties for the final sample of the MaNGA survey (∼10000 nearby galaxies; Abdurro'uf et al. 2022) as legacy products, but also to study the formation and evolution of galaxies with the combination of the dynamical and stellar population properties. In Paper I (Zhu et al. 2023), we performed the JAM (Cappellari 2008, 2020) on the full sample of MaNGA survey and obtained their quality-assessed dynamical properties. In Paper II (Lu et al. 2023), we performed SPS on the final MaNGA sample and obtained their global and spatially resolved stellar population properties, as well as their star formation histories.

This paper is the 5th paper of our MaNGA DynPop series. The goal of this paper is to understand the stellar initial mass function variation among galaxies. However, one can hardly study the IMF without understanding the DM content. Thus, in this work, we will combine the studies of the relation between the DM fraction and the stellar velocity dispersion, as well as the stellar initial mass function variation among galaxies from the currently largest integral field unit (IFU) spectroscope survey, MaNGA (Abdurro'uf et al. 2022). We will employ the dynamical modelling-based method to study the IMF variation by combining the dynamical modelling-based stellar mass-to-light ratio from Paper I and the stellar population synthesis-based stellar mass-to-light ratio from Paper II. Further, we will investigate whether the IMF variation signal inferred with the dynamical method can be confirmed with a spectral analysis of IMF. The readers are also referred to Paper III (Zhu et al. 2024) for a study of multiple dynamical scaling relations of these galaxies, Paper IV (Wang et al. 2024) for a study of the density profiles of galaxy groups and clusters, combining the stellar dynamical modelling and weak lensing, and Paper VI (Li et al. 2024) for a detailed comparison of total density slopes of galaxies between MaNGA and cosmological simulations.

This paper is organized as follows: In Section 2, we introduce the MaNGA project (Section 2.1), the structural and dynamical

properties (Section 2.2), the stellar population properties (Section 2.3) used in this paper, as well as the sample selection criteria which generate our final sample in this work (Section 2.4). Results on dark-stellar decomposition, initial mass function variation, and IMF-sensitive spectral feature analyses are shown in Section 3, Section 4, and Section 5, respectively. Finally, we present our discussions and conclusions in Sections 6 and 7, respectively.

2 DATA AND METHOD

2.1 MaNGA project

MaNGA (Bundy et al. 2015) currently stands as the largest IFU spectroscope survey in the world. MaNGA targets over 10 000 nearby galaxies within the redshift range of $0.01 < z < 0.15$ (Yan et al. 2016b; Wake et al. 2017), with the wavelength range of the spectra spanning from 3600 to 10300 Å and a spectral resolution of about $R \sim 2000$ (Drory et al. 2015; see Yan et al. 2016a for more details on MaNGA spectrophotometry calibration). Data products of the spectra are generated from the calibration and reduction on the raw data using the data reduction pipeline (DRP; Law et al. 2016). 67 per cent of the galaxies are observed out to $1.5R_e$ (where R_e is the effective radius of galaxies) and 33 per cent are observed out to $2.5R_e$, conducting the 'Primary+' and 'Secondary' samples, respectively (Bundy et al. 2015). Readers are referred to the following papers for more details on the MaNGA instrumentation (Drory et al. 2015), observing strategy (Law et al. 2015), spectrophotometric calibration (Smee et al. 2013; Yan et al. 2016a), and survey execution and initial data quality (Yan et al. 2016b). The MaNGA project is now finished and the complete data have been released (Abdurro'uf et al. 2022).

2.2 The axisymmetric Jeans anisotropic modelling

We obtain the structural and dynamical properties of the full MaNGA sample from the first paper of our MaNGA DynPop series (Paper I; Zhu et al. 2023). In Paper I, the axisymmetric JAM (Cappellari 2008, 2020) is applied to the complete sample of MaNGA to extract their quality-assessed structural and dynamical properties, using the PYTHON version of JAM, JAMPY.[1]

2.2.1 JAM mass models

Paper I provides the properties from JAM with different assumptions on the shape of dark haloes and velocity dispersion ellipsoids. In this work, we adopt the results with the cylindrically aligned velocity dispersion ellipsoid (Cappellari 2008) and compare the results under different mass model assumptions. The mass models adopted in this work include:

(i) The mass-follows-light model (MFL model hereafter; also know as the self-consistent model, e.g. Cappellari et al. 2013a; Shetty et al. 2020): The total mass distribution is assumed to follow the SDSS r-band (Stoughton et al. 2002) luminosity distribution of galaxies and no stellar–DM (DM) decomposition is applied.

(ii) JAM model with an NFW dark halo (NFW model hereafter): In this model, the total mass distribution consists with a oblate stellar component (following the SDSS r-band luminosity distribution by assuming a constant stellar mass-to-light ratio) and a spherical NFW dark halo (Navarro, Frenk & White 1997).

(iii) JAM model with a gNFW dark halo (gNFW model hereafter): This model is similar to the NFW model, but the dark halo is assumed to be a spherical gNFW model (Wyithe, Turner & Spergel 2001), which allows for the variation of the inner density slope γ of the dark halo (in NFW dark halo, it is set to be $\gamma = -1$).

In all JAM models, the supermassive black hole (SMBH) mass of galaxies is estimated with the $M_{BH}-\sigma_c$ relation from McConnell et al. (2011), where M_{BH} is the mass of the SMBH and σ_c is the stellar velocity dispersion within the aperture with radius being the full width at half-maximum (FWHM) of the MaNGA point spread function (PSF).

2.2.2 Structural and dynamical properties

Below, we briefly introduce the structural and dynamical properties of galaxies used in this work, all of which are taken from the catalogue of Paper I.

(i) Half-light radii: R_e^{maj} is the semimajor axis of the elliptical half-light isophotes of the galaxies. R_e satisfies $\pi R_e^2 = A$, where A is the area of the elliptical half-light isophote. The elliptical half-light isophote (i.e. the galaxy centre, the global ellipticity, and the sizes) is obtained with the PYTHON software, MGEFIT[2] by Cappellari (2002). The sizes are scaled by a factor of 1.35 to approximately match the popular galaxy sizes obtained from extrapolated photometry (see fig. 7 of Cappellari et al. 2013b).

(ii) σ_e is the luminosity-weighted velocity dispersion calculated within the elliptical half-light isophote. Specifically, it is calculated as

$$\sigma_e = \sqrt{\frac{\sum_k F_k(V_k^2 + \sigma_k^2)}{\sum_k F_k}}, \quad (1)$$

where V_k and σ_k are the mean line-of-sight velocity and dispersion in the k-th spaxel, respectively, and F_k is the corresponding flux. The summation goes over all the spaxels within the elliptical half-light isophote. Velocities and dispersion here are obtained by the MaNGA Data Analysis Pipeline (DAP; Belfiore et al. 2019; Westfall et al. 2019).

(iii) $(M/L)_{JAM}$ is the total mass-to-light ratio (including stellar and DM) of the galaxies.

(iv) $(M_*/L)_{JAM}$ is the stellar mass-to-light ratio of the galaxies.

(v) f_{DM} is the DM fraction within a sphere of radius R_e.

In this work, we take the total mass-to-light ratio from the MFL model and the other JAM-related properties (i.e. JAM-based stellar mass-to-light ratio and JAM-based DM fraction) from the NFW model. The NFW model is set as the default model of this work and the comparisons between JAM models are made in Section 4.2.1. The readers are referred to section 3.3 of Paper I for more details on mass model design of JAM.

2.3 Stellar population properties of galaxies

The stellar population properties used in this work are derived from the catalogue[3] in the second paper of our MaNGA DynPop series (Paper II; Lu et al. 2023). Paper II performs the Penalized Pixel-Fitting method (PPXF[4]; Cappellari & Emsellem 2004; Cappellari

[1] Version 6.3, available from https://pypi.org/project/jampy/

[2] Version 5.0.14, available from https://pypi.org/project/mgefit/

[3] Available from https://github.com/manga-dynpop

[4] Version 8.2, available from https://pypi.org/project/ppxf/.

2017, 2023) on the spectra produced by MaNGA DRP. As pointed out by Woo et al. (2024), PPXF is three to four times faster than other SPS codes, including FIREFLY (Wilkinson et al. 2017), PYPIPE3D (Sánchez et al. 2016a, b; Lacerda et al. 2022), and STARLIGHT (Cid Fernandes et al. 2005), and is the best in recovering stellar population properties among the four softwares. The SSP model used in Paper II is generated with the FSPS[5] software (Conroy, Gunn & White 2009; Conroy & Gunn 2010), combining the Salpeter (1955) IMF and the MIST isochrones (Choi et al. 2016). Specifically, the relevant stellar population properties in this work include:

(i) lg Age (keyword: `LW_Age_Re` from the catalogue of Paper II): lg Age is the global luminosity-weighted age of the galaxies, which is derived from the PPXF fitting on the stacked spectra within the elliptical half-light isophotes. With the best-fitted weights from PPXF, the luminosity-weighted age is defined as

$$x = \frac{\sum_k w_k L_k x_k}{\sum_k w_k L_k}, \tag{2}$$

where x here is lg Age; w_k and L_k are the best-fitted weight and the corresponding SDSS r-band luminosity of the k-th template, respectively.

(ii) [Z/H] (keyword: `LW_Metal_Re`): [Z/H] is the global luminosity-weighted metallicity of the galaxies, derived with the same way as the global age.

(iii) $(M_*/L)_{\rm SPS}$ (keyword: `ML_int_Re`): $(M_*/L)_{\rm SPS}$ used here is stellar mass-to-light ratio of galaxies, fitted from the stacked spectra within the elliptical half-light isophotes. It is defined as

$$(M_*/L)_{\rm SPS} = \frac{\sum_k w_k M_{*,k}}{\sum_k w_k L_k}, \tag{3}$$

where $M_{*,k}$ is the stellar mass (including the mass of living stars and stellar remnants, but excluding the gas lost during stellar evolution) and L_k is the corresponding luminosity of k-th templates. This quantity is *intrinsic* to the stellar population, being a unique function of the age and metallicity distribution of the stellar population. For this reason, it is independent of attenuation effects, which are accounted for during the PPXF fit. The summation goes over all the templates used in the fitting.

(iv) A_V (keyword: `Av_Re`): A_V is the average dust attenuation effect at $\lambda = 5500$ Å(V band) within the elliptical half-light isophote.

(v) f_{L_r} (keyword: `Fred_tot_Re`): f_{L_r} is the r-band luminosity ratio between the *observed* spectra and the *intrinsic* spectra, both of which are stacked within the elliptical half-light isophotes (see fig. 2 of Paper II for details).

(vi) $\gamma_{M_*/L}$ (keyword: `ML_int_Slope`): $\gamma_{M_*/L}$ is the gradient of *intrinsic* r-band stellar mass-to-light ratio within the elliptical half-light isophote.

We note here that although the mass-to-light ratios taken from Paper I and Paper II are measured in the same aperture, they are not comparable without further calibration. The SPS-based stellar mass-to-light ratio (derived from Paper II) is defined to be the 'intrinsic' values (i.e. dust attenuation effect independent; see Paper II for more details), while the JAM-based mass-to-light ratio (derived from Paper I) is estimated without correcting for the dust attenuation effect. Thus, before comparing the mass-to-light ratios from different methods and further constraining the initial mass function, we correct the JAM-based (total or stellar) mass-to-light ratio using the dust attenuation factor estimated from Paper II, with

$$(M/L)_{\rm JAM,corr.} = (M/L)_{\rm JAM,uncorr.} \times f_{L_r}, \tag{4}$$

where $(M/L)_{\rm JAM,\ uncorr.}$ is the uncorrected JAM-based mass-to-light ratio (either stellar or total mass-to-light ratios), directly taken from the catalogue of Paper I. f_{L_r} is the estimate of dust attenuation effect given by PPXF fitting (see Paper II for details). For simplicity, in following sections, the symbols, $(M_*/L)_{\rm JAM}$ and $(M/L)_{\rm JAM}$ are used only for the 'corrected' JAM-based stellar and total mass-to-light ratios, respectively. We emphasize here that such a reddening correction is only an approximation. The reddening effect is small, which only reduces the JAM-based mass-to-light ratios (and hence the stellar mass excess factor; see Section 4.2 for definition) by 0.13 dex (median value) for the Qual $\geqslant 1$ sample used in Section 3 and 0.08 dex for the high-quality ETGs used in Sections 4 and 5 (see Section 2.4 for sample selection criteria). Thus, the choice of reddening correction method will not qualitatively change the results in this work.

2.4 Sample selection

Combining the two catalogues from Zhu et al. (2023) (Paper I) and Lu et al. (2023) (Paper II), we get 9878 unique galaxies with available dynamical and stellar population properties. As stated in Paper I, galaxies are assigned with a quality flag, which indicates the reliability of the dynamical quantities (see table 2 of Paper I for details). In Section 3 of this work, we only take galaxies with Qual ≥ 1 (total mass estimates can be trusted) into account, which results in 5952 galaxies with different morphologies, in order to balance the sample size and the parameter reliability. In IMF-related analyses (i.e. Sections 4 and 5), however, stricter criteria should be applied. First, we only take galaxies with Qual $= 3$ (the highest quality) into account, which have the most reliable estimate of JAM-based stellar mass-to-light ratio of galaxies, resulting in 1129 galaxies with different morphologies. Secondly, we select the galaxies that satisfy:

$$\Delta \lg (M_*/L)_{\rm JAM} = \left| \lg(M_*/L)^{\rm cyl}_{\rm JAM} - \lg(M_*/L)^{\rm sph}_{\rm JAM} \right| < 0.05, \tag{5}$$

where $(M_*/L)^{\rm cyl}_{\rm JAM}$ and $(M_*/L)^{\rm sph}_{\rm JAM}$ are the stellar mass-to-light ratios from JAM with cylindrically (Cappellari 2008) and spherically aligned (Cappellari 2020) velocity dispersion ellipsoids, respectively, further resulting in 909 galaxies (we name these galaxies as the 'golden sample') out of 1142 Qual $= 3$ galaxies.

Measuring the IMF in external spiral galaxies is more challenging than in ETGs because the spectra of spirals are dominated by bright stars in their young stellar population. This makes it difficult to quantify the contribution of faint low-mass stars from their spectral features. Additionally, spiral galaxies contain large amounts of dust and multiple star formation events, which make the stellar population M_*/L more uncertain. As a result, both spectral features and dynamics/lensing methods are less reliable for measuring the IMF in spiral galaxies. For these reasons, most previous studies on IMF variation focus only on ETG or passive galaxy for both the spectral features method (e.g. van Dokkum & Conroy 2010; Spiniello et al. 2012) and the dynamical (e.g. Cappellari et al. 2012; Shetty et al. 2020) or lensing (e.g. Auger et al. 2010; Treu et al. 2010) methods. An exception is the work by Li et al. (2017), which tried to correct for dust and gas in MaNGA spiral galaxies with some empirical relations.

In this work, we also focus on ETGs in all our IMF-related analyses, except Section 4.2.2, where we show the comparison of IMF$-\sigma_{\rm e}$ relation under different sample selection criteria. To classify

[5]Available from https://github.com/cconroy20/fsps.

ETG and late-type galaxy, we employ the morphology catalogue from Domínguez Sánchez et al. (2022), which applied a deep-learning method to obtain the classification of morphologies of the full sample of MaNGA. Domínguez Sánchez et al. (2022) provided multiple classification criteria to select ETGs. Here, we simply take the galaxies with T-Type ≤ 0 as ETGs, resulting in 235 out of 909 galaxies in the golden sample. We confirm that our results would keep nearly unchanged when different morphology classification criteria are applied. In the following sections, we name this sample as the 'morphology-based sample'.

3 STELLAR MASS-TO-LIGHT RATIO AND DARK MATTER FRACTION

To study the IMF, one first needs to understand the variations of the DM fraction, which can give a similar effect as the IMF when the total and stellar mass distribution have similar profiles. We already presented trends of the DM fraction $f_{\rm DM}(< R_{\rm e})$ in Paper III as a function of stellar mass M_*. We also showed in fig. 16 therein that $f_{\rm DM}(< R_{\rm e})$ best correlates with $\sigma_{\rm e}$ rather than M_*. Here, we study the trends as a function of $\sigma_{\rm e}$ directly. Moreover, in addition to using the DM fraction inferred with JAM, we also make use of an alternative approach, based on comparing stellar population and dynamics, to strengthen our results.

3.1 Mass-to-light ratio versus velocity dispersion

In the top sub-figure of Fig. 1, we present the distributions of three different mass-to-light ratios as a function of $\sigma_{\rm e}$ from left to right for all the MaNGA galaxies with Qual $\geqslant 1$ (5952 galaxies[6]). The first ratio is the total mass-to-light ratio $(M/L)_{\rm JAM}$ inside a sphere of radius $R_{\rm e}$, which includes both stellar and DM and is obtained from JAM with an MFL model (see Section 2.2.1 for details of JAM model design). The second ratio is the stellar mass-to-light ratio $(M_*/L)_{\rm JAM}$, which is obtained from JAM with an NFW model. The third ratio is the average SPS-based stellar mass-to-light ratio $(M_*/L)_{\rm SPS}$ within the elliptical half-light isophote.

The left panel of the top sub-figure of Fig. 1 is the same as the top panel of Fig. 5 in Paper III, where a clear parabolic relation between $\lg(M/L)_{\rm JAM}$ and $\lg\sigma_{\rm e}$ is seen. The total mass-to-light ratio first slightly decreases with $\sigma_{\rm e}$ until $\lg(\sigma_{\rm e}/{\rm km\,s^{-1}}) \sim 1.89$ (from the best-fitted correlation in Paper III), and then increases with $\sigma_{\rm e}$. The JAM-based stellar mass-to-light ratio, $\lg(M_*/L)_{\rm JAM}$, however, does not show the same parabolic relation with $\lg\sigma_{\rm e}$ as the total mass-to-light ratio $\lg(M/L)_{\rm JAM}$, but shows roughly linear correlation with $\lg\sigma_{\rm e}$ (see the contours of its distribution and the figure for clipped sample in the bottom sub-figure). At the low $\sigma_{\rm e}$ end, $(M/L)_{\rm JAM}$ is significantly higher than $(M_*/L)_{\rm JAM}$, compared to larger velocity dispersions. This indicates that the DM in the inner region of galaxies (within about $1R_{\rm e}$) is more important for low $\sigma_{\rm e}$ galaxies. With increasing $\sigma_{\rm e}$, the difference between total mass-to-light ratio and JAM-based stellar mass-to-light ratio becomes smaller, until $\lg\sigma_{\rm e} \sim 2.25$, indicating the decrease of DM content in the inner region of the galaxies.

Crucially, the same approximately linear trend of logarithmic quantities (i.e. PL relation) is also seen for the SPS-based stellar mass-to-light ratio in the right panel of Fig. 1 (top panel). The consistent lack of a parabolic trend in both the $\lg(M_*/L)_{\rm SPS} - \lg\sigma_{\rm e}$ and $\lg(M_*/L)_{\rm JAM} - \lg\sigma_{\rm e}$ relations, combined with a clear parabolic trend in the $\lg(M/L)_{\rm JAM} - \lg\sigma_{\rm e}$ relation leaves no doubt about the reality of the trend of increasing DM starting below $\lg\sigma_{\rm e} \lesssim 2.1$.

It is also clear in the middle panel of Fig. 1 that there are a number of galaxies which strongly deviate from the main trend. The tail of galaxies with unrealistically low $\lg(M_*/L)_{\rm JAM} \lesssim -0.2$ must be the objects for which the DM is overestimated due to the degeneracy in the model parameters. The ones at the top with $\lg(M_*/L)_{\rm JAM} \gtrsim 1.1$ are likely face-on models, for which the stellar mass-to-light ratios tend to be overestimated (Lablanche et al. 2012). The existence of this clear $\lg(M_*/L)_{\rm JAM} - \lg\sigma_{\rm e}$ relation allows us to detect problematic models and remove them from the analysis that follows. Thus, in the bottom sub-figure of Fig. 1, we show the same distribution as the top sub-figure but for the sample for which we have excluded the outliers out of 3σ in order to show a cleaner trend. The clipping is performed on the $\lg\sigma_{\rm e} - \lg(M_*/L)_{\rm JAM}$ relation using the NDIMAGE.PERCENTILE_FILTER routine of the SCIPY software (Virtanen et al. 2020) and then the same clipped galaxies in the $\lg\sigma_{\rm e} - \lg(M_*/L)_{\rm JAM}$ relation are also excluded from the other two relations. There are 349 out of 5952 Qual $\geqslant 1$ galaxies clipped and we can see that the main trends we see in the top sub-figure remain unchanged.

In all panels, we also show the smoothed mean luminosity-weighted age from Paper II. It was computed with the LOESS_2D routine[7] of Cappellari et al. (2013b), which implements the multivariate LOESS algorithm of Cleveland & Devlin (1988). It is interesting to see that both the JAM-based total mass-to-light ratio, $(M/L)_{\rm JAM}$, and the JAM-based stellar mass-to-light ratio, $(M_*/L)_{\rm JAM}$ do not show correlation with age at fixed $\sigma_{\rm e}$, while the SPS-based stellar mass-to-light ratio shows strong age dependence at fixed $\sigma_{\rm e}$. The latter is expected as we already see similar distributions of age and SPS-based stellar mass-to-light ratio on the mass–size plane (e.g. Li et al. 2018 and Paper II), which implies the tight correlation between the two parameters. Cappellari et al. (2013b, fig. 1) pointed out that the JAM-based mass-to-light ratio also varies along the direction of $\sigma_{\rm e}$ on the mass–size plane, similar to the stellar population properties (i.e. age and SPS-based stellar mass-to-light ratio), but it is only for ETGs. We confirm that late-type galaxies do not show tight correlation between age from SPS and mass-to-light ratio from JAM, causing the lack of this correlation for the whole sample as shown in Fig. 1. This may be because that the high gas content of late-type galaxies contribute to the JAM-based mass-to-light ratio, washing out its correlation with age.

3.2 Dark matter versus velocity dispersion

Having qualitatively established the need for non-luminous matter at low $\sigma_{\rm e}$, now we can try to quantify it. Thus, in Fig. 2, we present the correlation between DM fraction (either derived from JAM or SPS) and velocity dispersion. The JAM-based DM fraction $f_{\rm DM}^{\rm JAM}$ is calculated with the sphere with radius $R_{\rm e}$, while the SPS-based DM fraction is calculated with the following approximation (Cappellari et al. 2013a, equation 22):

$$f_{\rm DM}^{\rm SPS} = 1 - \frac{(M_*/L)_{\rm SPS}}{(M/L)_{\rm JAM}}. \quad (6)$$

It relies on the empirical fact that $(M/L)_{\rm JAM} \approx (M/L)(< R_{\rm e})$, where $(M/L)_{\rm JAM}$ is measured from MFL models. In Paper I, we confirmed that, especially on low-quality data where it matters most, $(M/L)_{\rm JAM}$

[6]There are 6065 galaxies with Qual $\geqslant 1$ according to Zhu et al. (2023, table 2), among which 5952 have available SPS-based stellar mass-to-light ratio estimates.

[7]We used v2.1 available from https://pypi.org/project/loess/.

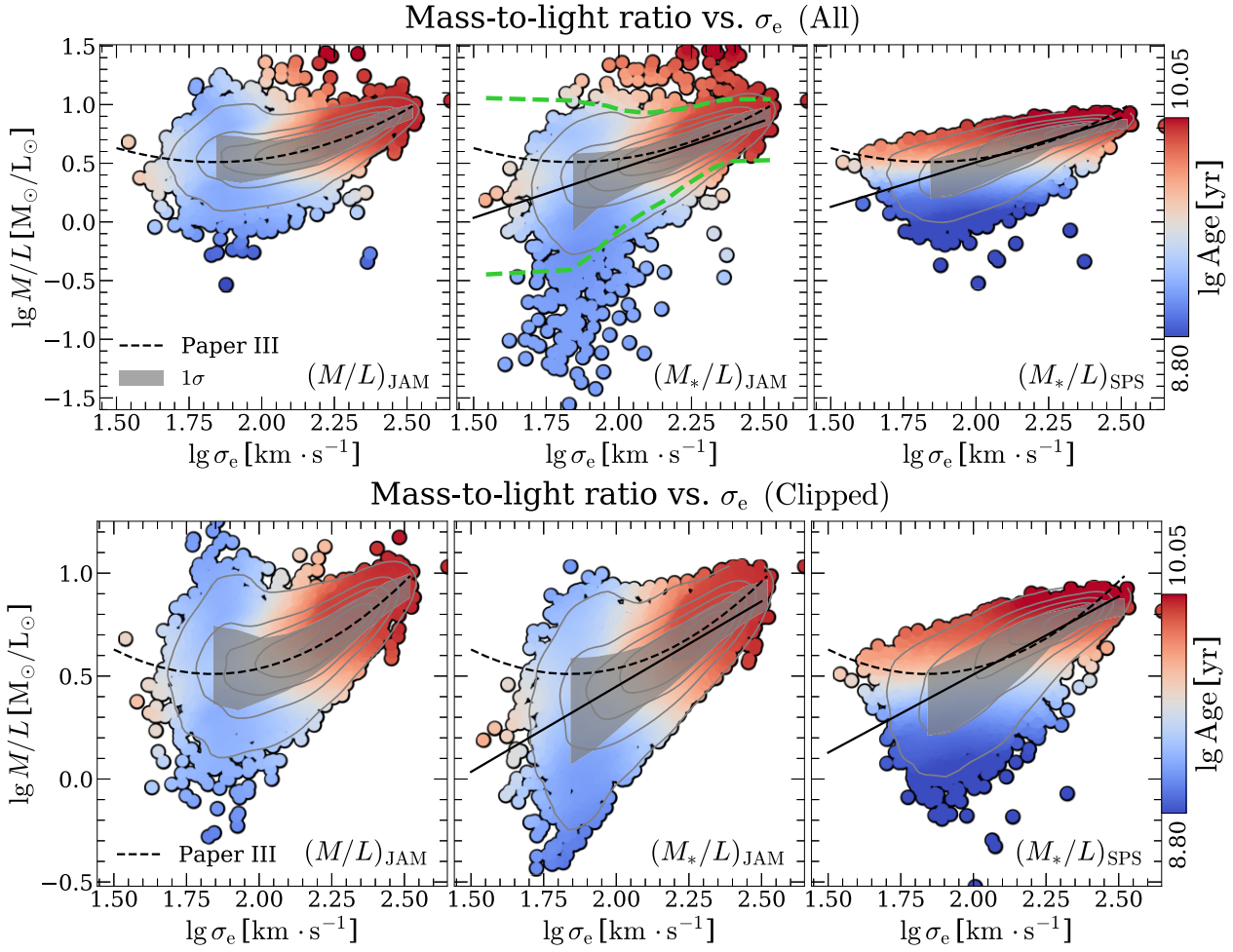

Figure 1. Top panel: the correlation between mass-to-light ratio and velocity dispersion of galaxies. Here, we included both spirals and ETGs models with Qual > 0. From left to right, we show the trend of (1) total (including stars and DM) mass-to-light ratio obtained with an MFL JAM model (see Section 2.2.1 for details of the models); (2) the stellar mass-to-light ratio obtained with an NFW JAM model; (3) the stellar mass-to-light ratio within the elliptical half-light isophote obtained with SPS. In each panel, the colours indicate the global luminosity-weighted age within the elliptical half-light isophote (see Section 2.3 for details). The black-dashed curve indicates the best-fitted parabolic relation between dynamical mass-to-light ratio and lg σ_e from Paper III. The solid black line indicates the best-fitted linear correlation between the stellar mass-to-light ratio and the velocity dispersion. The grey-shaded regions indicate the range from 16 to 84 percentiles ($\pm1\sigma$). The green-dashed curves in the middle panel indicate the 3σ region, out of which the galaxies are clipped. A kernel density estimation of the galaxy number density is indicated by the grey contours. Bottom panel: the same as the top sub-figure but the samples shown are clipped based on the lg $(M_*/L)_{JAM}$ − lg σ_e relation to exclude the outliers out of the 3σ region using the NDIMAGE. PERCENTILE_FILTER routine of the SCIPY software.

provides a more accurate estimate of $(M/L)(< R_e)$ than the value integrated from JAM models with DM.

As can be seen, the JAM-based DM fraction decreases with σ_e from ∼0.4 (median value) at lg $\sigma_e \sim 1.8$ to $f_{DM} < 0.1$ at lg $\sigma_e \sim 2.2$ and keep nearly constant afterwards, consistent with what we see in Fig. 1. This trend is also seen for the nearly independent SPS-based DM fraction, where SPS-based DM fraction is also higher at low σ_e. It reaches the lowest DM fraction at lg $\sigma_e \sim 2.2$ and then increases with increasing σ_e. We note that in this work, a fixed Salpeter IMF is assumed when obtaining the SPS-based stellar mass-to-light ratio. It overestimates $(M_*/L)_{SPS}$ at the low σ_e (thus underestimate the DM fraction) and underestimates $(M_*/L)_{SPS}$ at the high σ_e (thus overestimate the DM fraction) as the IMF varies with σ_e (e.g. van Dokkum & Conroy 2010; Cappellari et al. 2012 and Section 4 of this work). It also causes the negative SPS-based DM fractions at intermediate σ_e. Although there is stellar-DM degeneracy in dynamical modelling (see Li et al. 2016 for a quantitative investigation of the degeneracy in JAM with cosmological simulation), combining the trends of DM fraction and σ_e from JAM and SPS, we are still able to confirm the decreasing trend of DM fraction from low to high σ_e on a statistical basis. Again, we see that f_{DM}^{JAM} does not show correlation with galaxy age, while f_{DM}^{SPS} still shows age dependence even at fixed σ_e, which may be due to the gas contribution in the JAM-based mass-to-light ratio (and hence, the DM fraction).

Fig. 2 constitutes the most robust evidence so far for an increase of the DM fraction within R_e for decreasing velocity dispersion below lg $\sigma_e \lesssim 2.1$. Given that there is no evidence for the IMF to increase at low σ_e, the increase of f_{DM}^{SPS} provides a strong confirmation of the same trend in f_{DM}^{JAM}. The fact that $f_{DM}^{SPS} < f_{DM}^{JAM}$ must be due to the assumed Salpeter IMF which overestimates the stellar mass and consequently underestimates f_{DM}^{SPS} at low σ_e. We confirm that the f_{DM}^{SPS}-related results remain unchanged when $(M/L)_{JAM}$ used in equation (6) is replaced by the total mass-to-light ratio from JAM models with dark haloes (i.e. the NFW and gNFW models). Here,

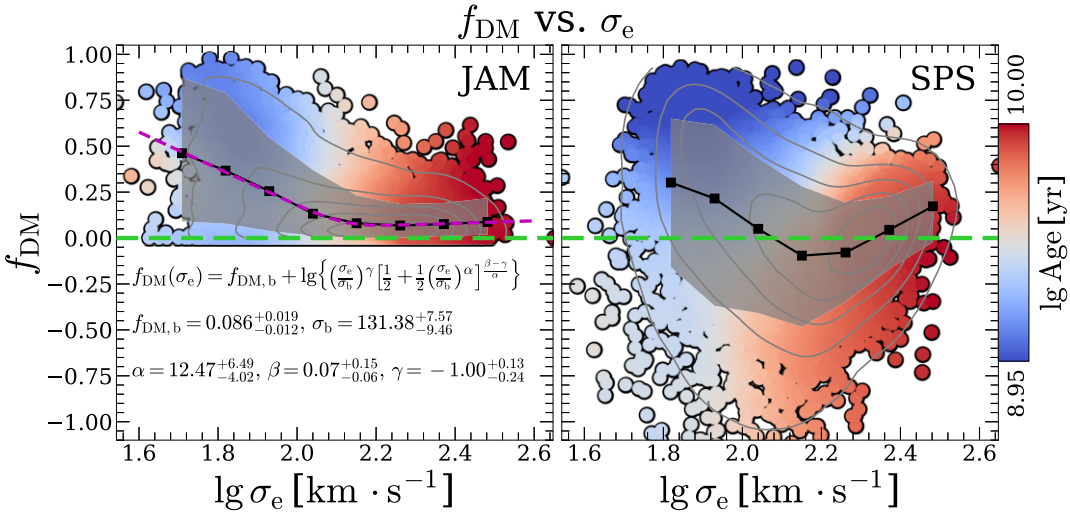

Figure 2. The correlation between DM fraction ($f_{\rm DM}$) and velocity dispersion of galaxies (the clipped sample from Fig. 1). The $f_{\rm DM}$ in the left panel is from JAM with an NFW model (estimated within a sphere with radius being $R_{\rm e}$; see Section 2.2.1 for details of JAM models). The $f_{\rm DM}$ in the right panel is simply calculates as $f_{\rm DM} = 1 - (M_*/L)_{\rm SPS}/(M/L)_{\rm JAM}$ (following Cappellari et al. 2013a, equation 22). In each panel, the colours indicate the global luminosity-weighted age of the galaxies (i.e. the average age within the elliptical half-light isophote; see Section 2.3 for details). The black squares and the black solid curve indicate the median trend of $f_{\rm DM}-\lg\,\sigma_{\rm e}$ relation, with the grey-shaded region indicating the 1σ region. A kernel density estimation of the galaxy number density is indicated by the grey contours. The green line indicates $f_{\rm DM} = 0$, below which the DM fraction is not applicable to JAM-based results. For the JAM-based DM fraction, we fit a double PL relation to the $f_{\rm DM}-\lg\,\sigma_{\rm e}$ correlation (the magenta-dashed curve) and the result is shown in the left panel.

Table 1. The best-fitted parameters of equation (7) and their measurement uncertainties derived using the bootstrap method.

$f_{\rm DM,\,b}$	$\sigma_{\rm b}$	α	β	γ
$0.086^{+0.019}_{-0.012}$	$131.38^{+7.57}_{-9.46}$	$12.47^{+6.49}_{-4.02}$	$0.07^{+0.15}_{-0.06}$	$-1.00^{+0.13}_{-0.24}$

we fit a double PL relation to the JAM-based $f_{\rm DM}-\lg\,\sigma_{\rm e}$ relation with the formula being:

$$f_{\rm DM}(\sigma_{\rm e}) = f_{\rm DM,b} + \lg\left\{\left(\frac{\sigma_{\rm e}}{\sigma_{\rm b}}\right)^{\gamma}\left[\frac{1}{2}+\frac{1}{2}\left(\frac{\sigma_{\rm e}}{\sigma_{\rm b}}\right)^{\alpha}\right]^{\frac{\beta-\gamma}{\alpha}}\right\}, \qquad (7)$$

where $\sigma_{\rm b}$ is the break value of $\sigma_{\rm e}$;$f_{\rm DM,\,b}$ is the DM fraction at the break $\sigma_{\rm b}$; α is the sharpness; β is the slope at large $\sigma_{\rm e}$; and γ is the slope at small $\sigma_{\rm e}$. We list the best-fitted values of the parameters in Table 1, together with their measurement uncertainties. The measurement uncertainties are derived using the bootstrap method, following the steps below:

(i) Randomly select half of the samples from the original data set (used in Fig. 2).

(ii) Calculate the median profile for the sub-sample and fit the same double PL relation as equation (7).

(iii) Repeat the above steps 500 times and calculate the 16th and 84th percentiles of the 500 best-fitted parameter sets.

3.3 Comparison with previous studies

Many previous studies have been made to investigate the DM content in different galaxies. For example, Toloba et al. (2014), using crude virial estimates of the galaxy masses, found that the DM fraction of dwarf early-type (dE) galaxies in the Virgo cluster is lower than the DM fraction of ETGs in Cappellari et al. (2013a). Tortora, La Barbera & Napolitano (2016) used spherical isotropic Jeans models and confirmed the results of Toloba et al. (2014) and further pointed out a decreasing trend of DM fraction with increasing velocity dispersion (see fig. 3 therein). Eftekhari et al. (2022) used the virial estimator and found that low-mass dwarf galaxies tend to have higher dynamical-to-stellar mass ratio (or equivalently, higher DM fraction) than high-mass dwarf galaxies with a larger sample. All these studies confirms the fact that DM becomes more important in low-mass galaxies. Eftekhari et al. (2022) interpreted it as the consequence of the stronger supernovae energy feedback and UV photoionization in lower mass haloes (see also Babul & Rees 1992; Martin 1999; Dekel & Woo 2003) which lowers the star formation efficiency therein. However, these studies are all based on the crude virial mass estimates. With accurate dynamical modelling, Cappellari et al. (2013a) also found that DM fraction increases with decreasing stellar mass for low-mass early-type ATLAS$^{\rm 3D}$ galaxies (see fig. 10 therein). Santucci et al. (2022) studied the DM content of SAMI galaxies (Bryant et al. 2015) with the Schwarzschild orbit-superposition models (Schwarzschild 1979) and also found the similar result (see fig. 7 therein). However, both studies focus only on the massive galaxies ($M_* \gtrsim 6\times10^9\,{\rm M}_\odot$ for Cappellari et al. 2013a and $\lg(M_*/{\rm M}_\odot) > 9.5$ for Santucci et al. 2022). Moreover, all previous studies studied DM correlations with M_*. But we found in Paper III that DM correlates better with stellar velocity dispersion than with stellar mass and for this reason we study correlations with $\sigma_{\rm e}$ here. It is the first time that the DM fraction variation is studied within such a wide velocity dispersion range ($1.6 \lesssim \lg\sigma_{\rm e} \lesssim 2.6$) with accurate dynamical modelling in such a large sample.

4 IMF VARIATION

4.1 IMF from the $M/L-\sigma$ relations

Fig. 2 already demonstrates, in qualitative manner and for a much larger sample, the main IMF trends that we will discuss more in detail later for our smaller golden sample: (i) the fact that for $\lg\,\sigma_{\rm e} \lesssim 2.3$, the median $f_{\rm DM}^{\rm SPS}$ becomes negative, indicates that the IMF must be

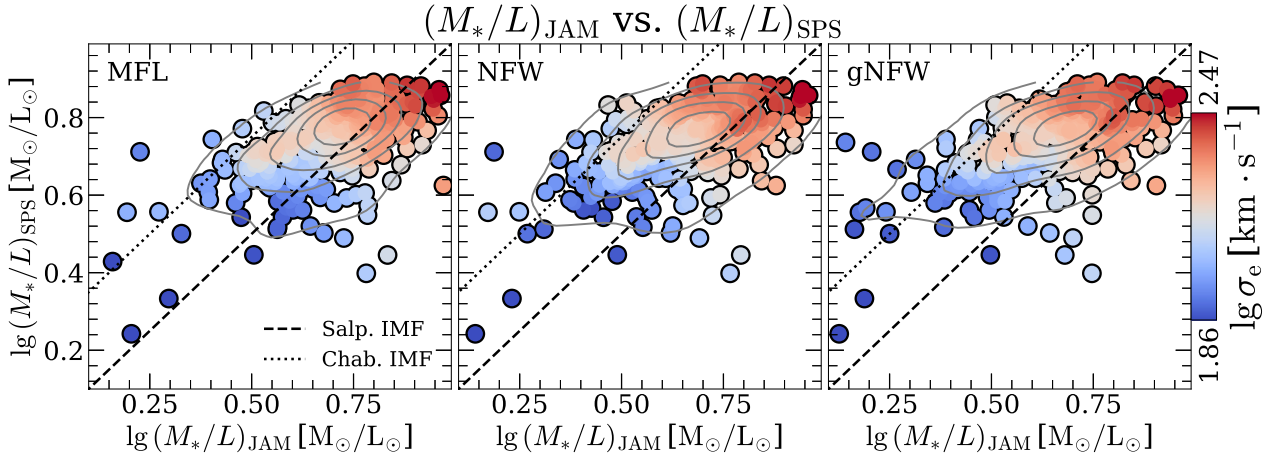

Figure 3. The comparison between the SPS-based stellar mass-to-light ratio and the JAM-based stellar mass-to-light ratio for the high-quality ETG sample. The results from JAM with the MFL model (for this model, we take its total mass-to-light ratio instead of the stellar one, as we do not separate stars and DM in this model), the NFW model, and the gNFW model are shown from left to right. In each panel, the colours indicate the velocity dispersion of the galaxies. The black-dotted line indicates the Chabrier IMF ($y = x + 0.25$) and the black-dashed line indicates the Salpeter IMF (adopted the SPS fitting; $y = x$). A kernel density estimation of the galaxy number density is indicated by the grey contours.

lighter than the adopted Salpeter IMF at those lower $\sigma_{\rm e}$, consistently with previous studies; (ii) the average $f_{\rm DM}^{\rm JAM}$ measured by JAM, which is independent of the stellar population, is nearly constant around $f_{\rm DM}^{\rm JAM} \approx 10$ per cent above $\lg\sigma_{\rm e} \gtrsim 2.1$, while the $f_{\rm DM}^{\rm SPS}$, assuming a Salpeter IMF, increases with $\sigma_{\rm e}$. Given that DM cannot explain the trend in $f_{\rm DM}^{\rm SPS}$, this suggests that the IMF becomes heavier with $\sigma_{\rm e}$. The variation $\Delta f_{\rm DM}^{\rm SPS} \approx 0.2$ from the minimum is similar to the expected M_*/L variation between a Salpeter and Chabrier IMF.

In Fig. 3, we present a direct comparison between the JAM-based and the SPS-based stellar mass-to-light ratios for the morphology-based sample (235 high-quality ETGs; see Section 2.4 for details of sample selection) for different JAM models (i.e. the MFL model,[8] the NFW model, and the gNFW model). As shown in the figure, for all the JAM models, galaxies with low stellar mass-to-light ratio typically have higher $(M_*/L)_{\rm SPS}$ than $(M_*/L)_{\rm JAM}$, consistent with Cappellari et al. (2012). Moreover, a similar trend is also seen for $\sigma_{\rm e}$, where we see galaxies with low $\sigma_{\rm e}$ have higher $(M_*/L)_{\rm SPS}$ than $(M_*/L)_{\rm JAM}$ (i.e. the assumed Salpeter IMF is heavier than reality). Regardless of its interpretation, the trend between the stellar population and dynamical stellar mass-to-light ratio is a robust and very general empirical result: Fig. 3 can be compared directly with Cappellari et al. (2013b, fig. 11) for the ATLAS$^{\rm 3D}$ sample in the local Universe and with Cappellari (2023, fig. 9) at redshift $z \approx 0.8$.

4.2 IMF versus velocity dispersion

In this section, we present the IMF variation as a function of velocity dispersion of galaxies. To quantify the IMF and its variation, we follow the practice of Treu et al. (2010), and define the stellar mass excess factor (also known as IMF mismatch parameter) as

$$\alpha_{\rm IMF} \equiv \frac{(M_*/L)_{\rm JAM}}{(M_*/L)_{\rm SPS}}, \tag{8}$$

where $(M_*/L)_{\rm JAM}$ and $(M_*/L)_{\rm SPS}$ are the stellar mass-to-light ratio estimated with JAM and SPS, respectively (see Sections 2.2 and 2.3 for details). Before making the comparison between the two stellar mass-to-light ratios, the JAM-based stellar mass-to-light ratio is corrected for the dust attenuation effect (both the dust influence from the MW and the galaxy itself; see Section 2.3 for more details) in order to be comparable with the SPS-based stellar mass-to-light ratio. The SPS-based stellar mass-to-light ratio employed here is fitted with a Salpeter (1955) IMF. Thus, $\alpha_{\rm IMF} = 1$ (or equivalently, $\lg\alpha_{\rm IMF} = 0$) indicates that JAM gives the same stellar mass estimate as SPS with a Salpeter (1955) IMF.[9]

4.2.1 *Comparison between JAM models*

In Fig. 4, we present the correlation between the stellar mass excess factor $\alpha_{\rm IMF}$ and velocity dispersion $\sigma_{\rm e}$ for three different JAM models (MFL, NFW, and gNFW; see sections 2.2.1 and 3.3 of Paper I for more details of the mass models). The galaxies used here are strictly selected ETGs, which have reliable JAM-based stellar mass-to-light ratio estimate (i.e. the morphology-based sample; see Section 2.4 for details of sample selection). All linear fittings in this paper are performed with the LtsFit package[10] described in Cappellari et al. (2013a). This tool combines the least Trimmed Squares robust technique of Rousseeuw & Driessen (2006) into a least-squares fitting algorithm which can account for errors in all variables, intrinsic scatter, and automatic outlier detection. As can be seen, a clear positive correlation between $\alpha_{\rm IMF}$ and $\sigma_{\rm e}$ is seen for all the three JAM models, confirming that galaxies with low $\sigma_{\rm e}$ tend to have Chabrier (2003) IMF (or even lighter), while high $\sigma_{\rm e}$ galaxies tend to have Salpeter (1955) IMF (or even heavier), consistent with previous studies (e.g. Cappellari et al. 2012, 2013b; Li et al. 2017; Shetty et al. 2020) with the same method.

$\alpha_{\rm IMF}$ from MFL model is systematically higher than those from NFW and gNFW models, as we did not separate stars and DM in MFL model (i.e. the 'stellar' mass-to-light ratio from MFL model is actually equivalent to the 'total' mass-to-light ratio of galaxies). The JAM-based mass-to-light ratio from MFL sets the upper limit

[8]For the MFL model, we take its total mass-to-light ratio instead of stellar mass-to-light ratio, as we do not separate stars and DM in this model.

[9]We will discuss more about this point in Section 6.1.

[10]Available from https://pypi.org/project/ltsfit/.

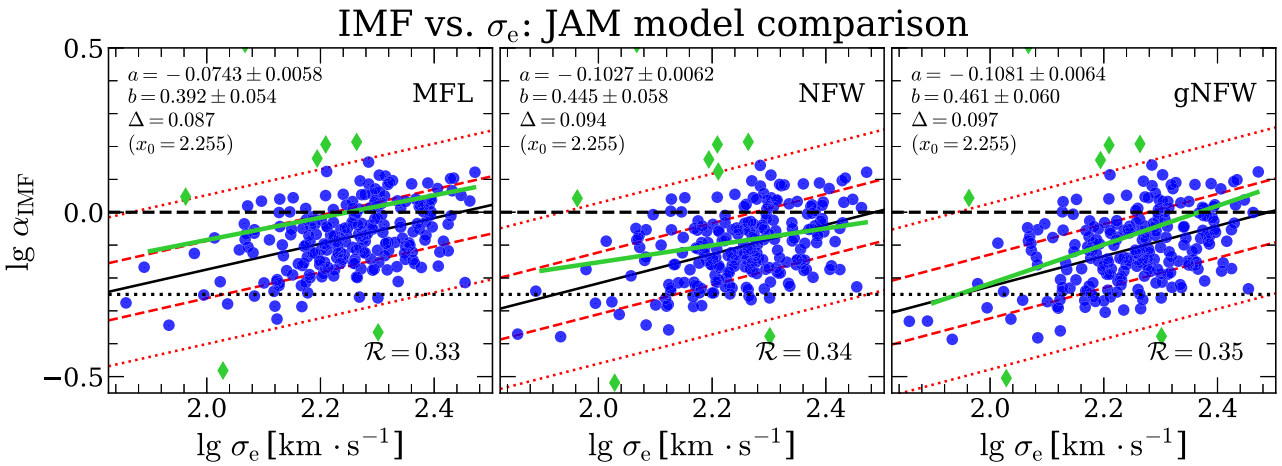

Figure 4. The correlation between α_{IMF} ($\equiv (M_*/L)_{JAM}/(M_*/L)_{SPS}$) and σ_e of selected high-quality ETGs for MFL, NFW, and gNFW models from left to right. In each panel, the blue dots are the galaxies used to fit the linear correlation and the green diamonds are the outliers excluded from the fit by the LTSFIT procedure (Cappellari et al. 2013a). The black solid line is the best-fitted lg σ_e– lg α_{IMF} obtained using the PPXF (Cappellari et al. 2013a) software. The red-dashed lines and dotted lines indicate the 1σ error (68 per cent) and 2.6σ error (99 per cent), respectively. The green solid line is the best-fitted correlation between α_{IMF} and σ_e from references with the same JAM mass model in each panel. The black-dashed line and the black-dotted line indicate the Salpeter (1955) and the Chabrier (2003) IMF. From left to right, the references are Shetty et al. (2020), Cappellari et al. (2013b), and Li et al. (2017). The best-fitted coefficients of the linear correlation $y = a + b(x - x_0)$ (where y is lg α_{IMF} and x is lg σ_e), the root-mean-square scatter Δ, and the Pearson correlation coefficient $\mathcal{R}$ are listed in each panel.

of stellar mass-to-light ratios from other JAM models. MFL model shows the flattest IMF–σ_e relation among the three investigated models. This is consistent with Fig. 1, where we see that at low σ_e end the mass-to-light ratio from MFL model (i.e. the total mass-to-light ratio) is obviously higher than those from NFW model (i.e. DM is more important at low σ_e; see also Fig. 2), while at high σ_e end the difference between MFL and NFW becomes smaller. This makes the stellar mass excess factors for MFL model is higher than that from stellar-DM decomposed models (i.e. NFW and gNFW model) at low σ_e, while is similar at high σ_e, making the $\sigma_e - \alpha_{IMF}$ trend for MFL model to be flatter. Interestingly, the IMF–σ_e relation under MFL model is slightly tighter than that under NFW/gNFW model, with the scatter being 0.087 dex (relative to 0.094 and 0.097 dex for NFW and gNFW models, respectively). This may be due to the stellar-DM degeneracy in dynamical modelling where the dynamical models always give only the *total* density, regardless of the modelling technique. The dark/luminous separation always depends on assumptions: the closer one assumes the shape of the stellar density traces the DM density, the strongest the degeneracy. This results in the more accurate estimate of *total* mass-to-light ratio (i.e. the mass-to-light ratio derived with an MFL model) than the stellar ones. The scatter discrepancy is also seen in Shetty et al. (2020, fig. 7), where the scatter of IMF–σ_e relation under self-consistent model (equivalent to the MFL model in this work) is also smaller than that under the model with an assumed dark halo. The observed scatter is comparable but slightly smaller than that $\Delta = 0.11$ dex in the ATLAS^{3D} models (Cappellari et al. 2013b). This may be due to the more uncertain relative distances for low-redshift galaxies or the more limited wavelength range of the ATLAS^{3D} reducing the accuracy of the population M_*/L. The scatter is instead slightly larger than the one $\Delta = 0.071$ for the Coma cluster study by Shetty et al. (2020), where relative distances are all accurately known and wavelength coverage is similar.

In each panel, we also plot the best-fitted results of previous studies with the same JAM mass model for comparison. In general, our results agree well with the results in previous studies within 1σ level and only show minor differences: α_{IMF} of Shetty et al. (2020) with MFL model is ~ 0.07 dex higher than our result with similar slope. The results from Cappellari et al. (2013b) (NFW model) and Li et al. (2017) (gNFW model) show slightly flatter and steeper correlation between α_{IMF} and σ_e, respectively, compared to our results. This confirms the robustness of our estimate of the stellar mass excess factor and again confirms the trend between stellar population and dynamical stellar mass estimates as a function of stellar velocity dispersion. This has been interpreted as due to the IMF variation among different galaxies.

4.2.2 *Comparison between sample selection criteria*

In this section, we study the impact of sample selection criteria on the IMF–σ_e relation. In the previous section, we select the ETGs for the IMF investigation due to the strong influence of dust and gas on stellar mass-to-light ratio in late-type galaxies (i.e. the morphology-based sample; see Section 2.4 for details). Actually, some other criteria can also be applied to reduce the negative influence of dust and gas in galaxies on the estimate of IMF, for example, selecting by age and dust attenuation factor. Thus, we further select two sub-samples from the golden sample (i.e. 909 galaxies with the most reliable estimates of JAM-based stellar mass-to-light ratio; see Section 2.4 for details):

(i) Dust-based sample: galaxies in this group are defined to be those with $A_V < 0.2$ (where A_V is the dust attenuation factor at $\lambda = 5500$ Å, i.e. V band), making up 340 galaxies among 909 galaxies in the golden sample.

(ii) Age-based sample: galaxies in this group are defined as the galaxies with lg Age > 9.7 in the golden sample, resulting in 394 galaxies out of 909 galaxies.

Besides, a constant stellar mass-to-light ratio is typically used in JAM, which, however, is not true under some circumstances (e.g. Ge et al. 2021). Paper II pointed out that galaxies in green valley exhibit strongly decreasing stellar mass-to-light ratio profiles from galaxy centre to the outskirts using stellar population synthesis. Paper

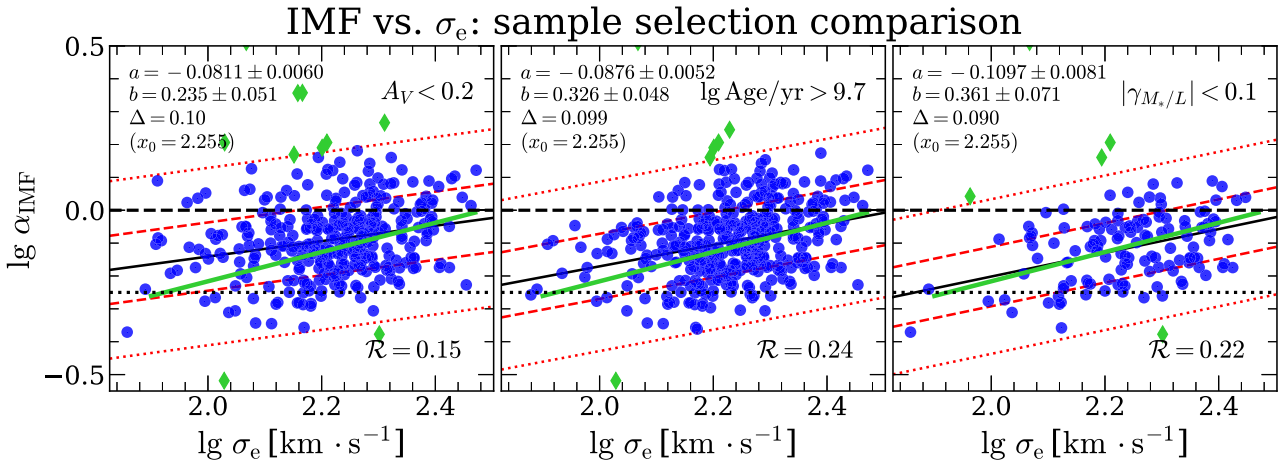

Figure 5. The correlation between $\alpha_{\rm IMF}$ and σ_e of the dust-based sample (left panel), the age-based sample (middle panel), and the $\gamma_{M_*/L}$-based sample (see Section 4.2.2 for definitions of the samples). In each panel, the green solid line is the best-fitted result of the high-quality ETG sample (with an NFW model). The other symbols are the same as Fig. 4. The best-fitted coefficients of the linear correlation $y = a + b(x - x_0)$ (where y is lg $\alpha_{\rm IMF}$ and x is lg σ_e), the root-mean-square scatter Δ, and the Pearson correlation coefficient $\mathcal{R}$ are listed in each panel.

III also pointed out that the assumption of constant stellar mass-to-light ratio in JAM influences on the estimate of DM fraction (see section 3.4.1 therein). Thus here, we investigate the possible influence of the constant-M_*/L assumption in JAM by selecting a sub-sample of galaxies with flat stellar mass-to-light ratio profiles on the morphology-based sample selected before:

(i) $\gamma_{M_*/L}$-based sample: galaxies in this group are the ones with $|\gamma_{M_*/L}| < 0.1$, making up 133 galaxies among 235 high-quality ETGs in the morphology-based sample.

In Fig. 5, we present the lg $\alpha_{\rm IMF}-$ lg σ_e relation for different samples described above. The JAM-based stellar mass-to-light ratio used here is under the NFW model (see Section 2.2 for details). As can be seen, the dust-based sample and age-based sample still show positive correlation between $\alpha_{\rm IMF}$ and σ_e, while the relations seem to be not as tight as the relation for the morphology-based sample (i.e. larger scatters and smaller Pearson correlation coefficient). The slopes of lg $\alpha_{\rm IMF}-$ lg σ_e relations with dust-based sample and age-based sample are both slightly smaller (i.e. flatter) than the morphology-based sample. Interestingly, the $\gamma_{M_*/L}$-based sample shows nearly the same lg $\alpha_{\rm IMF}-$ lg σ_e relation as its parent sample (i.e. the morphology-based sample), with only the tightness slightly increasing. This is consistent with Li et al. (2017), which also found that the positive lg $\alpha_{\rm IMF}-$ lg σ_e relation still exists when considering the stellar mass-to-light ratio gradient.

4.3 JAM models with general M_*/L gradients

We note that the stellar mass-to-light ratio gradients may be due to either the aging process and metallicity difference within individual galaxies (e.g. Li et al. 2018; Ge et al. 2021; see also our Paper II) or the radial gradient of initial mass function (e.g. van Dokkum et al. 2017; Parikh et al. 2018; La Barbera et al. 2019), the latter of which may have even stronger impact on the estimate of IMF with the dynamical modelling-based method (e.g. Bernardi et al. 2018, 2019, 2023; Domínguez Sánchez et al. 2019; Marsden et al. 2022, 2024). Thus, in this section, we present more discussion of the effect of constant–M_*/L assumption in JAM.

It has been argued that the presence of IMF gradients may bias the results of dynamical models that assume a constant IMF, and these gradients may artificially increase the observed IMF variations within $1R_e$ in galaxies (e.g. Bernardi et al. 2018; Domínguez Sánchez et al. 2019). The bias due to IMF gradients was suggested as a possible explanation for the disagreement between global IMF within $1R_e$ inferred from dynamics and population respectively (see review by Smith 2020). After the submission of our paper, similar claims were also made by Mehrgan et al. (2024).

To address these concerns, here we study the correlation between $\alpha_{\rm IMF}$ and σ_e while relaxing the constant stellar mass-to-light ratio assumption in the JAM models. For this, we build another JAM model in addition to the existing four mass models (i.e. MFL, NFW, gNFW, and fixed NFW models) in Paper I. The new model does not distinguish the stellar and DM components, but only parametrizes the total density. It is identical to Model (e) of Mitzkus, Cappellari & Walcher (2017) and Model I of Poci, Cappellari & McDermid (2017) and is characterized by a *total* density parametrized by a spherical generalized NFW profile (Wyithe et al. 2001):

$$\rho_{\rm tot}(r) = \rho_s \left(\frac{r}{r_s}\right)^{\gamma_{\rm PL}} \left(\frac{1}{2} + \frac{1}{2}\frac{r}{r_s}\right)^{-\gamma_{\rm PL}-3}. \quad (9)$$

Same as Paper I, the break radius r_s here is set to be $5 \times r_{\rm max,\,bin} < r_s < 250$ kpc, where $r_{\rm max,\,bin}$ is the largest radius of the galaxy where can be observed, to avoid unrealistic small/large r_s (see section 3.3.2 of Paper I for more details). With such a large break radius, the total density profile is nearly a PL within the region covered by the kinematics ($1.5-2.5R_e$ for MaNGA). Thus, we call the new model PL model hereafter. The stellar luminous tracer population is still described by the MGE parametrization of the observed surface brightness in the DynPop catalogue Paper I.

The PL model does not provide the stellar and dark mass separately but only returns the total density profile. Having the total mass profile and the luminosity profile, we are able to derive the total mass-to-light ratio profile and the average mass-to-light ratio within R_e. The PL model is analogous to the MFL model, for the fact that it also does not differentiate between luminous and DM. However, unlike the MFL model, the PL one is totally independent of any assumptions on the variation of the stellar mass-to-light ratios. The boundary of total density slope ($\gamma_{\rm PL}$) is set to range from –4 to 0, allowing for steeper total density slopes than the stellar ones (unlike our previous models). Thus, it is ideal to test for the effect of possible *M/L* gradients on the

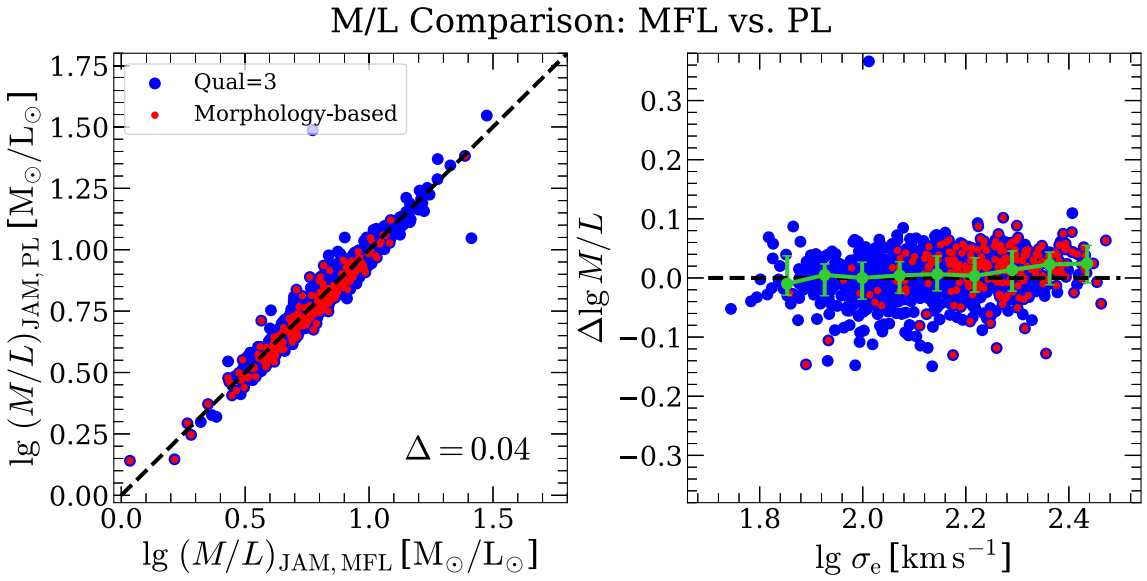

Figure 6. Left panel: the comparison between the total mass-to-light ratios from the PL model and the MFL model (see Section 2.2.1 for details). The blue dots are the galaxies with Qual = 3, and the red points denote the morphology-based sample, which is the default sample for IMF study in this work (see Section 2.4 for details). The black-dashed line indicates the $y = x$ relation. Right panel: trend of $\Delta \lg M/L$ ($\equiv \lg(M/L)_{\rm JAM,MFL} - \lg(M/L)_{\rm JAM,PL}$) as a function of velocity dispersion, $\sigma_{\rm e}$. The black-dashed line indicates $\Delta \lg M/L = 0$, and the green curve is the median trend for the Qual = 3 sample, with error bars indicating the range from 16th to 84th percentiles ($\pm 1\sigma$). These plots show that the total M/L is the same for the MFL models and for model that allows for density general gradients (i.e. the PL model; see Section 4.3 for more details).

recovered total M/L and the corresponding inferred trends of IMF among galaxies. The catalogue based on the PL model (including the total density slopes and the mass-to-light ratios) has been added to the JAM catalogue of Paper I. Readers can obtain the PL model catalogue through the journal website or access the full catalogue, consisting of five different JAM models, from the MaNGA DynPop website (https://manga-dynpop.github.io).

In Fig. 6, we show the comparison between the total mass-to-light ratios from the PL model, $(M/L)_{\rm JAM,\,PL}$ (which makes no assumption on the mass-to-light ratio gradients) and those from the MFL model, $(M/L)_{\rm JAM,\,MFL}$, (the mass-follows-light model, which assumes a constant mass-to-light ratio; see Paper I for more details), both of which are calculated within $R_{\rm e}$. For the PL models, we computed the $(M/L)_{\rm JAM,\,PL}$ by analytically integrating, within a sphere of radius $R_{\rm e}$, the MGEs of the best-fitting JAM models, using the `mge_radial_mass` procedure of the JAMPY package. As can be seen, the total mass-to-light ratios from the two models agree remarkably well with each other, without detectable bias and with a rms scatter of only 0.04 dex. In the right panel of Fig. 6, we show the correlation between the logarithmic difference $\Delta \lg(M/L) \equiv \lg(M/L)_{\rm JAM,MFL} - \lg(M/L)_{\rm JAM,PL}$ of the two total mass-to-light ratios and the velocity dispersion, $\sigma_{\rm e}$. As shown in the figure, $\Delta \lg(M/L)$ shows no obvious correlation with $\sigma_{\rm e}$. These results confirm that the constant mass-to-light ratio assumption used in JAM will not influence the estimate of the average mass-to-light ratio, at least within $R_{\rm e}$, within which we study the IMF variation among galaxies. This indicates that M/L gradients cannot be the reason for the observed trends in $\alpha_{\rm IMF}$

In Fig. 7, we showiig the correlation between $\alpha_{\rm IMF}$ based on PL model and $\sigma_{\rm e}$, and make comparisons with the MFL model. Again, we can see that the $\alpha_{\rm IMF}-\sigma_{\rm e}$ relation from PL model, which makes no assumption on mass-to-light ratios, agrees remarkably well with the result from MFL model, which assumes a constant mass-to-light ratio. This again confirms the robustness of the estimate of mass-to-

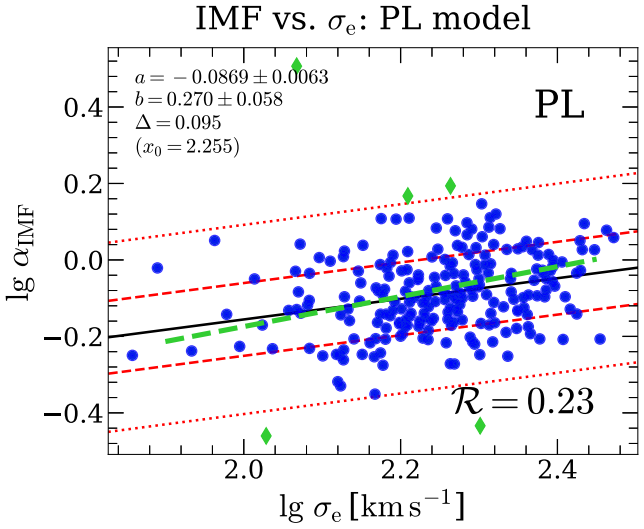

Figure 7. Correlation between lg $\alpha_{\rm IMF}$ (based on PL model) and lg $\sigma_{\rm e}$. The green-dashed line indicates the best-fitting relation from MFL model. The other symbols are the same as Fig. 4. The best-fitted coefficients of the linear correlation $y = a + b(x - x_0)$ (where y is lg $\alpha_{\rm IMF}$ and x is lg $\sigma_{\rm e}$), the root-mean-square scatter Δ, and the Pearson correlation coefficient $\mathcal{R}$ are listed.

light ratio within $R_{\rm e}$ under the constant M/L assumption. Note that the $\alpha_{\rm IMF}$ trends inferred with MFL or PL models only reflect the true IMF if DM is negligible. But we showed in this paper that this is indeed the case for the studied galaxies and that the $\alpha_{\rm IMF}$ trends are the same when considering the NFW or gNFW models (Fig. 4).

Our result contrasts with previous claims that M_*/L gradients strongly affect the inferred total M/L and may consequently spuriously drive the inferred IMF variations among galaxies (Bernardi

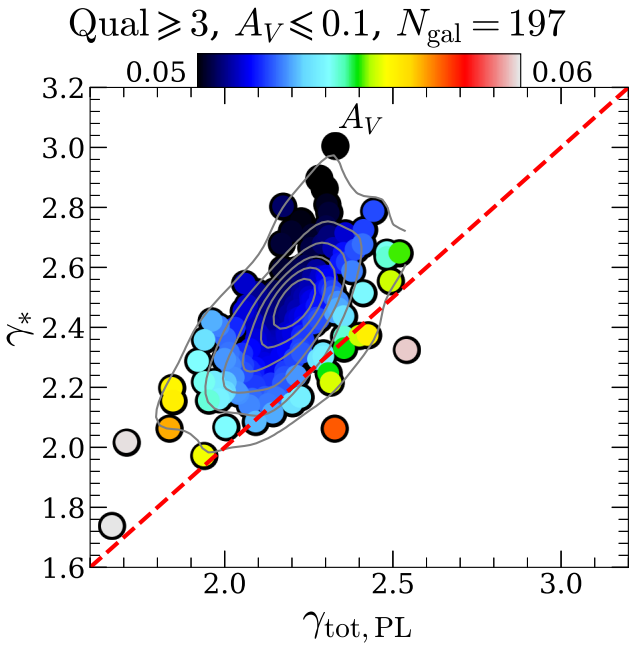

Figure 8. The comparison between the total density slope from PL model ($\gamma_{\rm tot,\,PL}$) and the stellar density slope (γ_*; same as the luminosity density slope, as the stellar mass-to-light ratio is assumed to be constant) within $R_{\rm e}$ for galaxies with Qual $\geqslant 3$ and $A_V \leq 0.1$ (see Section 2.3 for definition of A_V). The slopes are defined in equation (10). The colours of the points indicate A_V. The red-dashed line indicates $\gamma_{\rm tot,\,PL} = \gamma_*$. This plot indicates that the average *total M/L* decreases towards the centre within the studied region.

et al. 2018; Domínguez Sánchez et al. 2019). The reason for this disagreement is unclear and would require further investigation. However, both previous papers use an approximate approach to estimate the influence of IMF gradients, while here we model the galaxy dynamics in detail for every galaxy. This may be the reason for the differences.

More recently, Mehrgan et al. (2024) raised a similar concern as Bernardi et al. (2018) and Domínguez Sánchez et al. (2019), and pointed out that the constant-(M_*/L) assumption will increase the estimate of stellar mass by up to a factor of 1.5. They found that the model allowing for mass-to-light ratio gradient predicts lower stellar mass excess factor compared to the model with constant stellar *M/L* (see their figs 8 and 9). However, their study only considered seven galaxies. In addition, they calculated the integrated stellar mass excess factor α as the light-weighted $\alpha(r)$ across different radii, which is also different from the definition in our work (see equation 8). They found that the IMF inferred from their dynamical models becomes significantly heavier, and the total *M/L* increases towards the centre, within a region of radius $R \lesssim 1$ kpc.

To assess for the presence of gradients in the total *M/L* in our galaxies, in Fig. 8, we compare the total density slopes from the PL model $\gamma_{\rm tot,\,PL}$ against the stellar density slopes (same as the luminosity density slope when stellar *M/L* is assumed to be constant) γ_*. The (total/stellar) density slopes are defined as

$$\gamma = \frac{1}{\lg(R_{\rm e}/R_{\rm in})} \int_{R_{\rm in}}^{R_{\rm e}} \frac{{\rm d}\lg\rho}{{\rm d}\lg r} {\rm d}\lg r = \frac{\lg\rho(R_{\rm e}) - \lg\rho(R_{\rm in})}{\lg R_{\rm e} - \lg R_{\rm in}}, \qquad (10)$$

where $R_{\rm in}$ is the maximum between $0.1R_{\rm e}$ and the FWHM of MaNGA PSF; γ and ρ represent the total or stellar density slopes and radial densities, respectively.

Here, we select a subsample with the best dynamical models (i.e. Qual ≥ 3) and negligible dust extinction $A_V \leq 0.1$. We find that the total density slope is systematically smaller than the luminosity density. In other words, the total *M/L* decreases towards the centre within $1R_{\rm e}$. This decrease in *M/L* can be explained in two ways: (i) if DM is negligible, the decrease of the total *M/L* implies a decrease of the stellar M_*/L, or (ii) if DM dominates, the gradient would be due to an increase of DM with increasing radius. Given that several studies, including this paper, indicate that DM is likely negligible within $1R_{\rm e}$ in ETGs, option (i) seems favoured.

This may seem in contrast with results indicating IMF becoming heavier in galaxy centres. However, if the IMF becomes heavier only within a very small radius $R \lesssim 1$ kpc as suggested by Mehrgan et al. (2024), the effect would be undetectable by MaNGA, given that the relevant radius is generally contained within the FWHM of the PSF of the observations. Moreover, our PL approximation for the total density is likely to break down at such small scales, and not provide a good approximation for the total density profile. In other words, we cannot confirm or disprove the possible presence of a heavier IMF within $R \lesssim 1$ kpc.

To summarize, we find that the global trends with σ in $\alpha_{\rm IMF}$ that we infer from our models in Section 4.2 remain the same regardless of whether we allow for gradients in the total *M/L* (or IMF) or not.

4.4 IMF versus stellar population properties

In previous sections, we already see that the stellar mass excess factor, which constrains the IMF shape, shows positive correlation with velocity dispersion of galaxies. However, we still do not know whether $\sigma_{\rm e}$ is the main driver of IMF variation. In this section, we present the correlation between the stellar mass excess factor, $\alpha_{\rm IMF}$ and stellar population properties (including luminosity-weighted age, metallicity, and SPS-based stellar *M/L*; obtained from Paper II; see Section 2.3 for details) on the morphology-based sample (see Section 2.4 for selection details).

In Fig. 9, we present the correlation between $\alpha_{\rm IMF}$ and age, metallicity, and SPS-based stellar mass-to-light ratio from left to right. As can be seen, $\alpha_{\rm IMF}$ show positive correlation with lg Age, consistent with McDermid et al. (2014), with the slope slightly larger (steeper) than that of McDermid et al. (2014). Metallicity, again similar to McDermid et al. (2014), does not show obvious correlation with $\alpha_{\rm IMF}$ (low Pearson correlation coefficient). A positive correlation between $\alpha_{\rm IMF}$ and SPS-based stellar mass-to-light ratio is also seen for the galaxies. Compared to these correlations, the IMF$-\sigma_{\rm e}$ relation is obviously stronger and tighter, indicating that $\sigma_{\rm e}$ is more likely the main driving factor of IMF variation among galaxies, compared to stellar population properties.

We note, however, this is inconsistent with the studies which made use of the gravity-sensitive absorption lines, for example, $\rm Na_I$ doublet and FeH (also known as the Wing-Ford band) or the full spectrum fitting to study the IMF shape as a function of metallicity (e.g. Conroy & van Dokkum 2012; Martín-Navarro et al. 2015b; Zhou et al. 2019; Gu et al. 2022). They found an obvious correlation between IMF shape and metallicity, which may be even more responsible for the IMF variation than $\sigma_{\rm e}$ (e.g. Zhou et al. 2019). Smith (2014) studied this discrepancy between different methods with the stellar mass excess factors derived from dynamical modelling and spectrum analyses on the same sample. They found that although the stellar mass-to-light ratios derived in different methods both show positive correlation with velocity dispersion, there is no correlation between $\alpha_{\rm IMF}$ inferred from the two approaches on a galaxy-by-galaxy basis. They explained this as that one (or both) of the methods has not accounted fully for

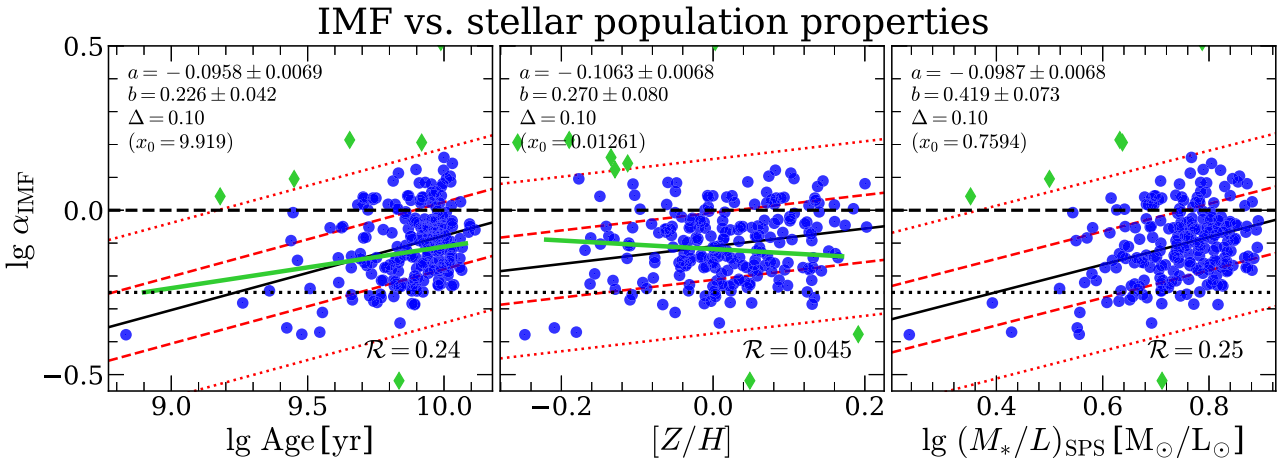

Figure 9. The correlation between $\alpha_{\rm IMF}$ and stellar population properties (age, metallicity, and stellar mass-to-light ratio from left to right) for the high-quality ETG sample (under the NFW mass model). In the left and middle panels, the green solid lines are the results from McDermid et al. (2014). The Pearson correlation coefficient is listed in each panel.

the main confounding factors and there is additional variation in the detailed shape of the IMF which cannot currently be inferred from the spectroscopic features. This remains a major crucial and worrying inconsistency between the different approaches. We will discuss it later in Section 6.2.

5 IMF-SENSITIVE SPECTRAL FEATURES

Smith (2020) suggested that one possibility to explain the inconsistent stellar mass excess factors derived with dynamical modelling and spectrum analysis is the aperture difference in which the stellar mass excess factors are measured, combined with radial gradients in the IMF: The dynamical modelling-based one is an average value within a sphere of approximately $1R_{\rm e}$, while the spectrum-based one is measured within $R_{\rm e}/8$. Thus, in this section, we combine the dynamical properties from Paper I and the stellar population properties from Paper II, which are, by design, measured in the same aperture (i.e. the elliptical half-light isophotes), to study whether galaxies with high and low dynamical modelling-based $\alpha_{\rm IMF}$ show corresponding spectral differences. It is worth remembering that formally, the dynamics infers average *M*/*L* inside a sphere of radius $R_{\rm e}$, while the stellar population measures average *M*/*L* inside a projected (elliptical) cylinder of radius $R_{\rm e}$. In our comparison, we ignore the likely small bias introduced by stars falling within the cylinder but outside the sphere of radius $R_{\rm e}$.

To make the investigation, we first select four sub-samples from 235 high-quality ETGs in the morphology-based sample (see Section 2.4 for details). Each of them contains two sub-groups with different dynamical $\alpha_{\rm IMF}$, with the criteria being:

(i) Sub-sample 1 (SS1): galaxies in this sub-sample are defined to have similar $\sigma_{\rm e}$, i.e. $2.15 < \lg(\sigma_{\rm e}/{\rm km\,s^{-1}}) < 2.25$. Then the high-$\alpha_{\rm IMF}$ (low-$\alpha_{\rm IMF}$) sub-group is further defined as those with the highest (lowest) 30 per cent $\alpha_{\rm IMF}$ within the $\sigma_{\rm e}$ bin, resulting in 21 galaxies in each sub-group.

(ii) Sub-sample 2 (SS2): galaxies in this sub-sample are similar with SS1, but within a $\sigma_{\rm e}$ range from $\lg(\sigma_{\rm e}/{\rm km\,s^{-1}}) = 2.25$ to $\lg(\sigma_{\rm e}/{\rm km\,s^{-1}}) = 2.35$, resulting in 25 galaxies in both the sub-group with high $\alpha_{\rm IMF}$ and the one with low $\alpha_{\rm IMF}$.

(iii) Sub-sample 3 (SS3): the high-$\alpha_{\rm IMF}$ (low-$\alpha_{\rm IMF}$) sub-group in this sub-sample contains the galaxies whose $\alpha_{\rm IMF}$ is 1σ higher (lower) than the best-fitted $\alpha_{\rm IMF}-\sigma_{\rm e}$ correlation, resulting in 47 galaxies with high $\alpha_{\rm IMF}$ and 43 galaxies with low $\alpha_{\rm IMF}$.

(iv) Sub-sample 4 (SS4): the high-$\alpha_{\rm IMF}$ (low-$\alpha_{\rm IMF}$) sub-group in this sub-sample contains the galaxies whose $\alpha_{\rm IMF}$ is the highest (lowest) 30 per cent among all the galaxies, regardless of $\sigma_{\rm e}$, resulting in 71 galaxies with high and low $\alpha_{\rm IMF}$.

To better demonstrate the sample selection, we present, in Fig. 10 (the top panels), the distributions of the selected galaxies on the ($\sigma_{\rm e}$, $\alpha_{\rm IMF}$) plane for the four sub-samples. The relevant information of these four sub-samples are also listed in Table 2. Having the samples, we then stack the spectra of the galaxies in the same sub-group for further investigation following the practice of Parikh et al. (2018). The steps are as follows:

(i) For a single galaxy, the spectrum in each spaxel is corrected to the rest frame with the corresponding redshift from NASA Sloan Atlas catalogue (Blanton et al. 2011) and the corresponding line-of-sight velocity provided by the MaNGA DAP (Belfiore et al. 2019; Westfall et al. 2019), using

$$\lambda_{\rm res} = \frac{\lambda}{(1+z)\cdot(1+\frac{v}{c})}, \tag{11}$$

where λ is the uncorrected (i.e. observed) wavelength; z is the redshift of the galaxy; v is the line-of-sight velocity of the spaxel[11]; c is the light speed. The spectra used here are from the MaNGA DRP (Law et al. 2016) (under the names being `manga-[PLATE]-[IFUDESIGN]-LOGCUBE.fits`).

(ii) The spectrum of each spaxel is interpolated to a common wavelength grid, keeping the spectrum resolution unchanged.

(iii) Spectra within the elliptical half-light isophote of one individual galaxy are simply co-added, without normalization. This produces one stacked 'effective spectrum' per galaxy.

(iv) The effective spectra of different galaxies are normalized with the mean flux within the wavelength range 6780–6867 Å, in order

[11]The velocities are obtained from the files under `manga-[PLATE]-[IFUDESIGN]-MAPS-SPX-MILESHC-MASTARSSP.fits`. We note that the velocity estimates of the pixel at the outskirts of the galaxies would be inaccurate without being binned to higher S/N ratio. Here, we only stack the spectra within $1R_{\rm e}$ and as a result, this effect would not largely change our results.

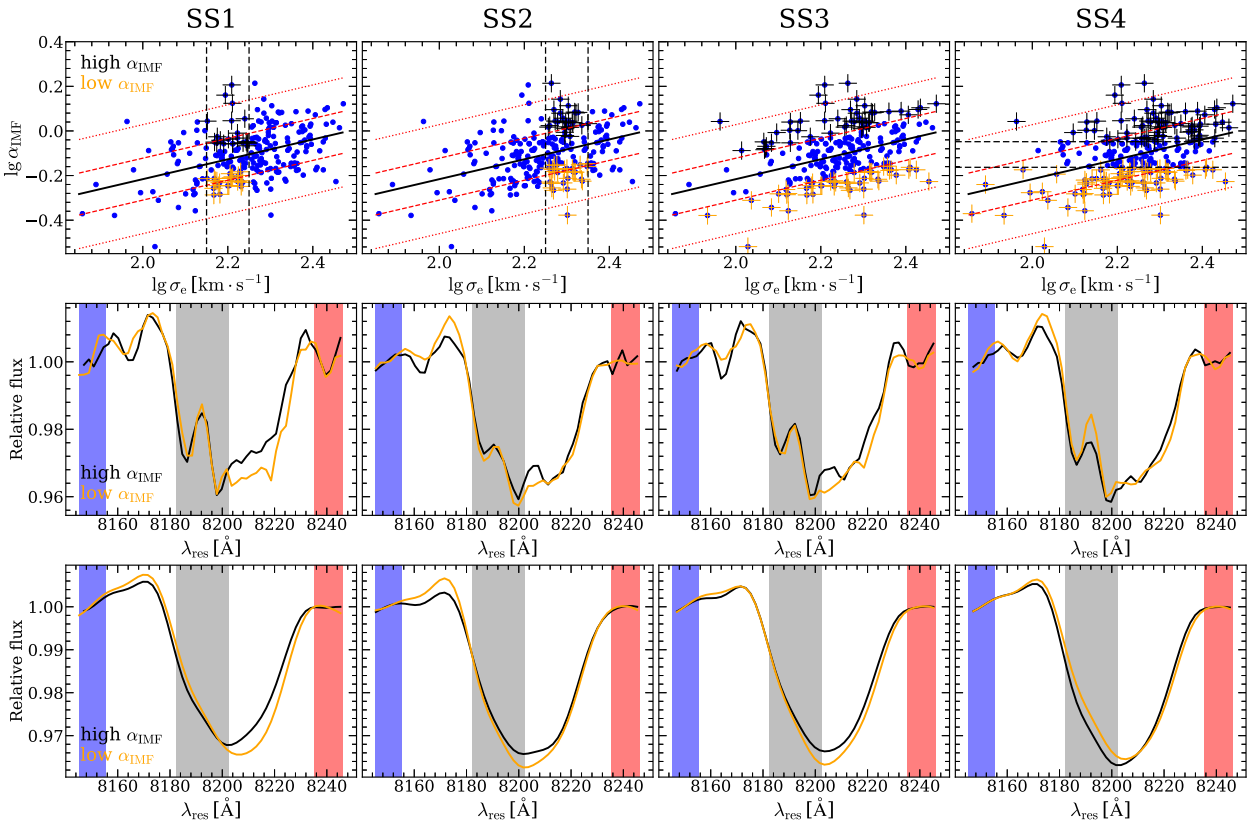

Figure 10. Top panel: The sample selections of SS1-SS4 from left to right (see Section 5 for definitions of the samples). In each panel, the parent sample is indicated by the blue dots (high-quality ETG sample, with an NFW mass model). The galaxies selected as high $\alpha_{\rm IMF}$ and low $\alpha_{\rm IMF}$ galaxies are indicated by black and orange plus symbols, respectively. In the first and second panel of the top row, the dashed vertical lines indicate the $\sigma_{\rm e}$ range, in which the samples are selected. In the fourth panel of the first row, the dashed horizontal lines indicate the lower (upper) $\alpha_{\rm IMF}$ boundary of the high (low) $\alpha_{\rm IMF}$ sample. Middle panel: the comparison of $\rm Na_I$ absorption line between the stacked spectra with high (black) and low (orange) $\alpha_{\rm IMF}$. Before plotting, the absorption feature is corrected for the local continuum (see Section 5 for the definition of the local continuum). In each panel, the red and blue regions are the pseudo-continuum regions defined in La Barbera et al. (2013) and the grey band is the region of the feature. Bottom panel: the same as the middle row, while the spectra are smoothed to 250 km s^{-1} for visualization purpose.

Table 2. Numbers of galaxies in different sub-samples. See Section 2.4 for the selection criteria. $N_{\rm gal}$ is the number of galaxies of each sub-group. S/N is the signal-to-noise ratio of the $\rm Na_I$ feature (8182.2 –8202.3 Å) of the stacked spectrum. lg $\alpha_{\rm IMF,avr}$ is the average stellar mass excess factor of the sub-group. σ_0 is the velocity dispersion of the stacked spectrum.

Sub-sample	Sub-group	$N_{\rm gal}$	S/N	lg $\alpha_{\rm IMF,avr}$	σ_0 (km s^{-1})
SS1	High $\alpha_{\rm IMF}$	21	2863	0.00	147.4
	Low $\alpha_{\rm IMF}$	21	2951	− 0.23	137.9
SS2	High $\alpha_{\rm IMF}$	25	4289	0.05	167.0
	Low $\alpha_{\rm IMF}$	25	4011	− 0.20	172.2
SS3	High $\alpha_{\rm IMF}$	47	9428	0.07	144.8
	Low $\alpha_{\rm IMF}$	43	7708	− 0.24	149.6
SS4	High $\alpha_{\rm IMF}$	71	14 433	0.05	170.6
	Low $\alpha_{\rm IMF}$	71	17 376	− 0.23	138.9

to account for the variation in fluxes from galaxy to galaxy. After that, the normalized effective spectra of the galaxies within the same sub-group are further co-added.

The stacked spectra so derived wash out the contamination of sky lines in the near-infrared (NIR) region of the spectrum, where the IMF-sensitive spectral features (i.e. $\rm Na_I$ and FeH) exist. Here, we define the noise of the stacked spectra as $\sigma/\sqrt{N_{\rm gal}}$, where σ is the standard deviation of the normalized flux of the spectra for stacking at specific wavelength and $N_{\rm gal}$ is the number of the galaxies stacked together. Parikh et al. (2018) tried to use both the $\rm Na_I$ doublet and the FeH line to constrain the IMF of MaNGA galaxies but they found that the results based on the FeH line have large uncertainties. They argued that it is because the FeH feature is faint, compared to the bright sky lines in this region, making the small uncertainties in sky subtraction unable to cancel out in the stacked spectra. Thus, in this work, we only use the $\rm Na_I$ doublet to constrain the IMF shape in this study. As mentioned in van Dokkum & Conroy (2012), $\rm Na_I$ line for a fixed Na elemental abundance is only present in low-mass stars, and hence is able to constrain the richness of the low-mass stars: the stronger the $\rm Na_I$ line, the more bottom heavy the IMF is. The wavelength range of the $\rm Na_I$ doublet, as well as the corresponding blue and red pseudo-continuum bandpasses are defined in La Barbera et al. (2013). In Table 2, we list the average S/N of $\rm Na_I$ doublet for different sub-groups. As can be seen, with such stacking processes, the S/N of the stacked spectra reaches a significantly high value, which allows for the spectral study of IMF.

We note here that in this work, we do not attempt to make detailed analysis on the IMF-sensitive spectral features, as done in previous studies (e.g. Conroy & van Dokkum 2012; Spiniello et al. 2012; van Dokkum & Conroy 2012; La Barbera et al. 2013; Spiniello

et al. 2015; Parikh et al. 2018). We only want to see whether the galaxies with different dynamical $\alpha_{\rm IMF}$ show various IMF-sensitive spectral features, which confirm their IMF difference in a model-independent manner. In the middle panels of Fig. 10, we present the comparison of $\rm Na_I$ doublets between the stacked high $\alpha_{\rm IMF}$ spectrum and the low $\alpha_{\rm IMF}$ spectrum for the four different sub-samples. Before overplotting, we first correct for the continuum shape of the spectrum and extract the absorption feature. The continuum is defined following the practice of Worthey et al. (1994): We first calculate the average flux in the blue and red pseudo-continuum bandpasses, using equation (2) of Worthey et al. (1994). The local continuum is then defined by taking a straight line from the blue pseudo-continuum to the red pseudo-continuum. The relative flux of the absorption feature is calculated as the ratio between the true flux at a given wavelength and the flux of the local continuum at the same wavelength. For visualization, we further smooth the $\rm Na_I$ lines to $\sigma = 250\,{\rm km\,s^{-1}}$ in the bottom panels of Fig. 10. As can be seen, all the stacked spectra show clear $\rm Na_I$ absorption features and the doublet is washed out at high σ. Comparing the $\rm Na_I$ absorption features of galaxies in the high $\alpha_{\rm IMF}$ sub-group (black curves) and in the low $\alpha_{\rm IMF}$ sub-group (orange curves) in the same sub-sample, we find that the difference between the two spectra are quite small and highly depend on the sample selection. The stacked spectrum with high $\alpha_{\rm IMF}$ (black) of SS1 shows slightly stronger $\rm Na_I$ absorption feature than the low $\alpha_{\rm IMF}$ (orange). The difference is more significant in SS4, where more galaxies are stacked and a higher S/N is reached. In SS2 and SS3, however, we see the opposite trend, where the stacked spectra with low $\alpha_{\rm IMF}$ (orange) show stronger $\rm Na_I$ absorption signals than the high $\alpha_{\rm IMF}$ ones. For sure, the variation we see is not comparable to the one illustrated fig. 1 of van Dokkum & Conroy (2010). If the dynamically determined $\alpha_{\rm IMF}$ variations are due to an IMF variation, the spectral features excludes the possibility for the IMF to vary from Chabrier to even heavier than Salpeter, as a number of studies originally suggested.

To quantitatively describe the difference of $\rm Na_I$ absorption strength, we calculate the equivalent width of the $\rm Na_I$ absorption feature with the method described in Worthey et al. (1994) (see equations 2 and 3 therein). To build up the connection between $\rm Na_I$ equivalent width and the IMF shape, we take the values from Parikh et al. (2018) (tables B1–B3) as references. The estimate of the equivalent widths of absorption lines always require a correction to homogenize all spectra to the same stellar velocity dispersion (e.g. Kuntschner 2004). Thus, to make the comparison between the $\rm Na_I$ equivalent widths of our spectra and those from Parikh et al. (2018), which are calculated at $\sigma = 100\,{\rm km\,s^{-1}}$, we have to first correct our $\rm Na_I$ equivalent widths to the same dispersion. Parikh et al. (2018) (also Westfall et al. 2019) convolved the best-fitted templates to obtain the $\rm Na_I$ equivalent width at the given velocity dispersion, while the templates used in this work do not have such high resolution, making it impossible to correct the equivalent widths with a simple convolution process. Here, we correct the $\rm Na_I$ equivalent widths following the steps below:

(i) For each stacked spectrum, we estimate its dispersion (σ_0; typically larger than $100\,{\rm km\,s^{-1}}$) using PPXF, allowing both the additive and multiplicative polynomials by setting `degree=mdegree = 4`.

(ii) We smooth the stacked spectrum to larger dispersions and calculate the corresponding $\rm Na_I$ equivalent widths at every $20\,{\rm km\,s^{-1}}$.

(iii) Finally, we perform a linear fit to the correlation using the LTSFIT software (Cappellari et al. 2013a) and calculate the predicted $\rm Na_I$ equivalent width at $\sigma = 100\,{\rm km\,s^{-1}}$.

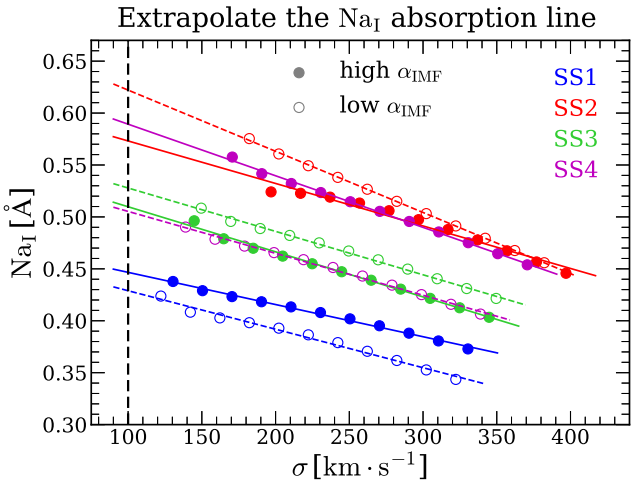

Figure 11. The illustration of correcting the equivalent width of $\rm Na_I$ to $\sigma = 100\,{\rm km\,s^{-1}}$. Results for different samples (SS1–SS4; see Section 5 for details of sample selection) are indicated by different colours. Filled and open circles denote the results of the spectrum with high and low $\alpha_{\rm IMF}$, respectively. The solid and dashed lines indicate the corresponding best-fitted $\rm Na_I$–σ linear relations, fitted with the LTSFIT (Cappellari et al. 2013a) software. The black-dashed line indicates $\sigma = 100\,{\rm km\,s^{-1}}$.

(iv) To derive the measurement uncertainty of the corrected $\rm Na_I$ equivalent widths, we employ a Monte Carlo-based method, following the practice of Parikh et al. (2018). Specifically, we perturb the flux at each wavelength with a number randomly taken from a Gaussian with its standard deviation equaling to the error in the flux at each pixel. Then the equivalent width is calculated and corrected to $\sigma = 100\,{\rm km\,s^{-1}}$. This is done for 500 times and the measurement uncertainty is measured as the standard deviation of the 500 $\rm Na_I$ equivalent widths.

The correlation between σ and the corresponding $\rm Na_I$ equivalent widths is shown in Fig. 11. As can be seen, this correlation can be well described by a linear relation, indicating the robustness of our extrapolation. In the top panels of Fig. 12, we overplot the reference values of $\rm Na_I$ equivalent widths from Parikh et al. (2018) and the corresponding IMF slopes against the corrected $\rm Na_I$ equivalent widths of this work. As can be seen, IMF slopes show positive correlation with $\rm Na_I$ equivalent width for both models adopted in Parikh et al. (2018) (red and blue symbols; see section 2.4 therein for details of the two models). For SS1, we find that both the high $\alpha_{\rm IMF}$ spectrum and the low $\alpha_{\rm IMF}$ spectrum show a Kroupa-like (Kroupa 2001) (or even lighter) IMF, which is inconsistent with what their average $\alpha_{\rm IMF}$ indicates (lg $\alpha_{\rm IMF,avr} = 0$ for high $\alpha_{\rm IMF}$ sub-group, indicating a Salpeter IMF). The high $\alpha_{\rm IMF}$ spectrum shows higher $\rm Na_I$ equivalent width than the low $\alpha_{\rm IMF}$, consistent with what we see in Fig. 10. SS4 galaxies show larger difference between the high $\alpha_{\rm IMF}$ and the low $\alpha_{\rm IMF}$ spectra, where high $\alpha_{\rm IMF}$ spectrum appears to have a Salpeter-like IMF (under the VCJ model) and the low $\alpha_{\rm IMF}$ spectrum appear to have a Kroupa-like IMF, consistent with what the average $\alpha_{\rm IMF}$ indicates. For SS2 and SS3, however, we again see the opposite trend for the two spectra.

Saglia et al. (2002) pointed out that the IMF shape and chemical abundances play a complex role in affecting the NIR features. Actually, the equivalent width of $\rm Na_I$ is not only affected by the IMF shape, but also by the abundance of sodium (e.g. Parikh et al. 2018). For example, Jeong et al. (2013) reported that a sodium abundance dependent on $\sigma_{\rm e}$ could also mimic an IMF variation.

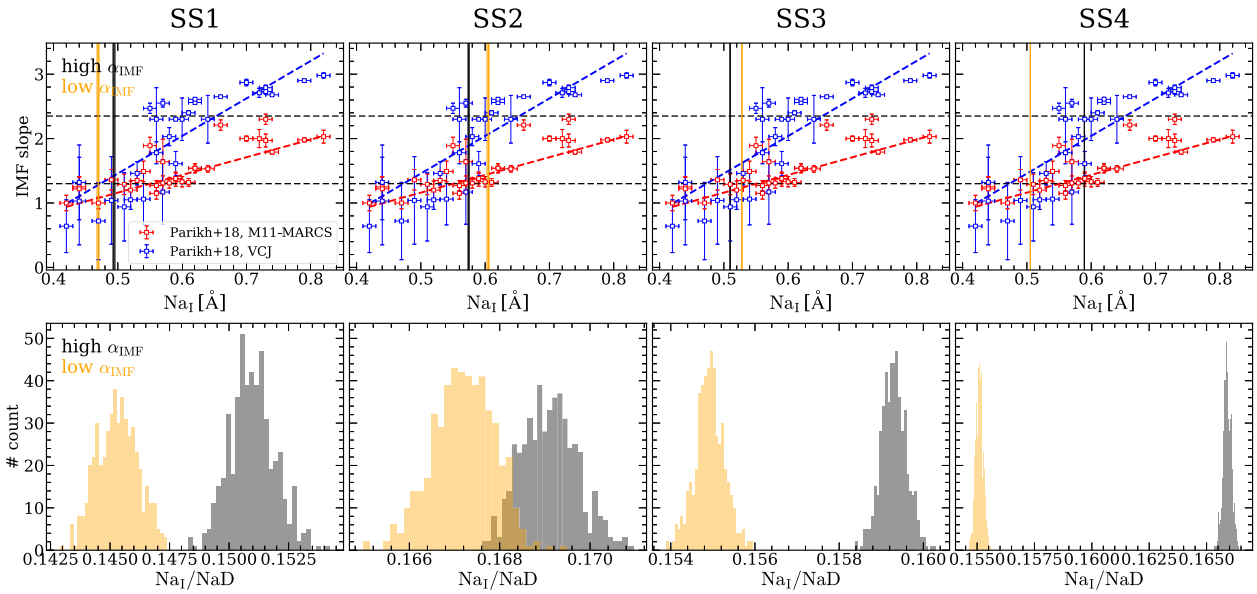

Figure 12. Top panel: correlation between IMF slope (within the mass range $0.1 - 0.5\,M_\odot$) and the corrected Na_I equivalent widths (at $\sigma = 100\,km\,s^{-1}$). The reference values are taken from Parikh et al. (2018) and the red and blue data points indicate the results from different methods (see Parikh et al. 2018 for details). In each panel, the blue- and red-dashed lines indicate the best-fitted linear relation between IMF slope and Na_I equivalent width, obtained with LTSFIT software (Cappellari et al. 2013a). The black and orange vertical lines refer to the Na_I equivalent widths of our stacked spectra, with the shaded region indicating the 1σ region obtained with a Monte Carlo-base method (see Section 5 for details). The Salpeter (1955) IMF and the Kroupa (2001) IMF are shown with the horizontal black-dashed lines from top to bottom. Bottom panel: the distributions of the Na_I/NaD ratio for the high α_{IMF} galaxies (black) and low α_{IMF} galaxies (orange). For each stacked spectra, the distribution of Na_I/NaD is obtained through a Monte Carlo-base method (see Section 5 for details) and both features are corrected to $\sigma = 100\,km\,s^{-1}$.

Here, we employ the equivalent width of NaD, which is sensitive to the sodium abundance and thus a good indicator, to account for the influence of sodium abundance on the Na_I–IMF relation. The feature region and the corresponding blue and red pseudo-continuum of NaD are defined in Trager et al. (1998). The equivalent width of NaD is calculated following the same steps of Na_I and is also corrected to $\sigma = 100\,km\,s^{-1}$. In the bottom panels of Fig. 12, we show the distributions of Na_I/NaD for high and low α_{IMF} spectra. The distributions are also obtained with a Monte Carlo-based method mentioned above. As can be seen, unlike the Na_I-IMF, all the spectra with high α_{IMF} show higher Na_I/NaD ratio than their low α_{IMF} counterparts. This trend is even stronger for the spectra stacked with more galaxies (i.e. SS3 and SS4). It implies that, when accounting for the influence of sodium abundance, galaxies with different dynamical α_{IMF} do show different IMF-sensitive features (i.e. the Na_I doublet) by stacking a number of galaxies together.

In summary, our analysis of the stellar absorption features presented in this section is not necessarily inconsistent with the variation of the dynamically determined α_{IMF} being due to a variation of the IMF from Chabrier-like to Salpeter-like as a function of σ_e. However, it is undeniable that the spectra with different α_{IMF} in Fig. 10 look strikingly similar and a small trend only emerges from careful analysis of subtle effects. Moreover, we have to rely on a single IMF-sensitive spectral feature, which could be partially affected by abundance variation (although we try to asses it). The combination of these facts does not make the result from spectral features conclusive. The problem is that the models themselves predict barely detectable differences in the line depths ($\lesssim 0.3$ per cent) between a Kroupa/Chabrier-like and Salpeter-like IMF at fixed chemical abundance (the reader is strongly encouraged to look at van Dokkum & Conroy 2010, fig. 1c). Earlier studies from spectral features suggested significantly more bottom-heavy IMF than Salpeter, which would have been easier to detect, both with the dynamical and spectroscopic methods. However, our work excludes such extreme IMFs, at least for the mean galaxy population at fixed velocity dispersion.

6 IMF DISCUSSION

We show in this discussion that there are ways to explain both (i) the lack of correlation between the *M/L* predicted from the dynamics and from the population and (ii) the lack of correlation between IMF and metallicity from dynamics, combined with a clear correlation between IMF and metallicity from spectral features. However, explaining both facts requires some unlikely conspiracies. If we were to apply Occam's razor, a simpler explanation would be that either the dynamics, or the population, or both, do not truly measure the weight of IMF. Of course, this still would require one to explain why this is the case, for which we do not have a satisfactory explanation either.

6.1 Top or bottom-heavy IMF?

The high stellar mass excess factor can be either due to the bottom-heavy IMF, which generates more low-mass stars (and hence produces a higher stellar mass-to-light ratio), or the top-heavy IMF, producing more massive stars, which are dead shortly after birth and thus contribute to the stellar mass but do not contribute to the luminosity. Barber, Crain & Schaye (2018) and Barber, Schaye & Crain (2019a, b) built up a hydrodynamical cosmological simulation upon the original EAGLE Simulation (Schaye et al. 2015) to study the possible influence of variable IMF, by allowing the IMF to be changed according to the gas pressure. They confirmed that both top-variable and bottom-variable IMFs are able to reproduce the stellar mass excess factor-σ_e relation presented in Cappellari et al. (2013b).

However, the analyses on gravity-sensitive spectral features (e.g. Na_I and FeH) can only put constraints on the IMF slope at low-mass end (typically $m < 0.5\,M_\odot$; e.g. van Dokkum & Conroy 2010; La Barbera et al. 2013; Parikh et al. 2018). Thus, the higher dynamics-based α_{IMF} at high σ_e does not necessarily mean high dwarf star enrichment (i.e. bottom-heavy IMF; see Smith 2020 for a review). A conspiracy between high-mass and low-mass part of the IMF (e.g. Lyubenova et al. 2016, and more recently, den Brok et al. 2024) may explain why, on the galaxy-by-galaxy basis, the stellar mass excess factors from dynamical methods do not match those from spectral feature analysis (Smith 2014).

6.2 Lack of IMF–metallicity relation from dynamics

It is intuitive that the IMF shape correlates with metallicity of galaxies, as the metallicty has impact on the cooling rate of the molecular clouds, which thus influence the relative numbers of the newly formed stars of different masses. With analyses on the gravity-sensitive spectral features (e.g. Na_I and FeH) and the full spectra, the correlation between metallicity and IMF shape has been firmly detected (e.g. Conroy & van Dokkum 2012; Zhou et al. 2019; Gu et al. 2022). However, as mentioned in the previous section, the IMF constraints so derived are only for the low-mass end of the IMF shape (i.e. $m \lesssim 0.5\,M_\odot$). Actually, the slope of the IMF at high-mass end also varies with the metallicity of galaxies. For example, Marks et al. (2012) found that with increasing metallicity, IMF becomes more top-light, by observing the Galactic globular clusters. Yan, Jerabkova & Kroupa (2017) (see fig. B1 therein; and see also Yan, Jeřábková & Kroupa 2021) also found the similar decreasing trend of IMF top slope (getting steeper, i.e. more top-light) with increasing metallicity. Thus, combining the IMF studies on the low-mass end (e.g. van Dokkum & Conroy 2010; Parikh et al. 2018) and on the high-mass end (e.g. Marks et al. 2012; Yan et al. 2017), we find that the initial mass function of galaxies gets more bottom-heavy and top-light with increasing metallicity, the former of which results in higher stellar mass excess factor, while the latter results in the lower. This could qualitatively (at least partially) explain why we cannot see the correlation between the dynamics-based stellar mass excess factor and metallicity of galaxies. We note here that the metallicity dependence of IMF slope at the high-mass end is somehow weak and may not be able to fully account for the absence of (dynamics-based) stellar mass excess factor–metallicity correlation. To solve this problem, we need a more detailed galaxy formation model which simulates the co-evolution of IMF and metallicity (e.g. fig. 5 of Yan et al. 2019). A hydrodynamical cosmological simulation, which enables the IMF variation may also help.

7 CONCLUSION

This work is the 5th paper of our MaNGA DynPop (dynamics and stellar population) series (see Lu et al. 2023; Zhu et al. 2023, 2024; Wang et al. 2024; for the other papers of this series). In this work, we study the DM fraction and initial mass function (IMF) variations among the galaxies in the final data release of MaNGA project (Abdurro'uf et al. 2022). Specifically, we take the dynamically determined stellar mass-to-light ratio with JAM (Cappellari 2008, 2020) from the first paper of MaNGA DynPop series (Zhu et al. 2023) and the stellar mass-to-light ratio with stellar population synthesis from the second paper of MaNGA DynPop (Lu et al. 2023) (assuming a Salpeter IMF), which are, by design, estimated within the same aperture, and hence are suitable for this study. In addition, we construct a new JAM dynamical model that relaxes the assumption of a constant stellar M_*/L, to assess the sensitivity of our results to the possible presence of IMF gradients.

By selecting a sub-sample of galaxies with the best dynamical modelling quality, and calculating the stellar mass excess factors (i.e. the ratio between the stellar mass-to-light ratios from two different methods; see equation 8 for definition), we are able to study the correlations between IMF and galaxy properties (e.g. velocity dispersion, age, metallicity, and SPS-based stellar mass-to-light ratio). Further, we also investigate the possible spectral difference between galaxies with high and low stellar mass excess factors. The main conclusions of this work are summarized as follows:

(i) The total (including stars and DM; obtained from JAM with an MFL model) mass-to-light ratio $\lg(M/L)_{JAM}$ within a sphere of radius $1R_e$ shows a parabolic correlation with the velocity dispersion of galaxies $\lg\sigma_e$, while the stellar mass-to-light ratios, both $\lg(M_*/L)_{JAM}$ from JAM and $\lg(M_*/L)_{SPS}$ from SPS, prefer a linear relation (Fig. 1). The large difference between total mass-to-light ratio and stellar mass-to-light ratio at low σ_e indicates a clear rise of the DM fraction within $1R_e$ towards low σ_e, which is confirmed in Fig. 2. We also provide an empirical relation between JAM-based DM fraction (within a sphere with radius being R_e) and $\lg\sigma_e$ (see equation 7 and Table 1).

(ii) SPS-based stellar mass-to-light ratio of low σ_e (and low $(M_*/L)_{JAM}$) galaxies is higher than JAM-based stellar mass-to-light ratio, indicating that the assumed Salpeter IMF is too heavy for low σ_e galaxies. On the contrary, galaxies with high σ_e and high $(M_*/L)_{JAM}$ have higher $(M_*/L)_{JAM}$ than $(M_*/L)_{SPS}$, indicating that the assumed Salpeter IMF is too light for those galaxies (Fig. 3). This is consistent with the findings in Cappellari et al. (2012).

(iii) The stellar mass excess factor, α_{IMF} shows positive correlation with velocity dispersion, σ_e, indicating that galaxies with $\lg\sigma_e \lesssim 2.0$ tend to have Chabrier-like (or even lighter) IMF, while those with high σ_e tend to have Salpeter-like IMF. This is consistent with the previous findings in which the similar approach is adopted (e.g. Cappellari et al. 2013b; Li et al. 2017; Shetty et al. 2020). With different dynamical models (see Section 2.2.1 for the definition of the models), the positive correlation is still seen, but with the slope of the trend slightly changing. The mass-follows-light model (MFL), which has the fewest free parameters gives the tightest $\lg\alpha_{IMF} - \lg\sigma_e$ relation (with the scatter being 0.087), while the gNFW model shows the largest scatter ($\Delta = 0.097$; see Fig. 4).

(iv) The $\lg\alpha_{IMF} - \lg\sigma_e$ relation is sensitive to the sample selection criteria. Apart from selecting galaxies according to their morphologies (the default choice of this work), we also select galaxies based on their dust attenuation effect (i.e. $A_V < 0.2$, where A_V is the dust attenuation effect at V band, i.e. $\lambda = 5500$ Å) and global age (i.e. $\lg$ Age/yr > 9.7). We find that, although the positive correlation between α_{IMF} and σ_e is still seen, the slopes of the correlation are shallower and the scatters are larger, compared to the galaxy sample selected according to their morphologies (i.e. the morphology-based sample; Fig. 5).

(v) By selecting a sample of ETGs with low stellar mass-to-light ratio gradient (i.e. $|\gamma_{M_*/L}| < 0.1$), we study the influence of the constant M_*/L assumption in JAM on the $\lg\alpha_{IMF} - \lg\sigma_e$ relation. We find that the $\lg\alpha_{IMF} - \lg\sigma_e$ relation does not show obvious difference from the parent sample (i.e. the morphology-based sample; Fig. 5). Further, with a new JAM model which makes no assumption on the M/L (see Section 4.3), we investigate the effect of the possible IMF radial variation within individual galaxies on our results. We show that the inferred α_{IMF} trend cannot be driven by radial gradients of

M_*/L (with fixed IMF) or IMF. We also find no evidence for the total M/L increasing toward the centre within $1R_e$ (Figs 6–8).

(vi) Positive correlation between α_{IMF} and age and stellar M/L is observed, indicating that galaxies with older age and higher stellar M/L are more likely to have heavier IMF, consistent with previous studies (Cappellari et al. 2012; McDermid et al. 2014). No obvious correlation between α_{IMF} and metallicity is seen (Fig. 9), consistent with McDermid et al. (2014), but inconsistent with those with a spectroscopic method (e.g. Conroy & van Dokkum 2012; Zhou et al. 2019). This long-standing crucial discrepancy may indicates that either the dynamical modelling-based method or the spectroscopic method or both, may not be measuring the IMF after all.

(vii) By stacking the spectra of galaxies with high α_{IMF} and low α_{IMF}, we study the Na_I difference (which is sensitive to the IMF shape at low-mass end) between the samples with different (dynamical modelling based) IMFs. A clear result is the strikingly similarity of the stacked spectra around the Na_I feature. Any small difference highly depends on the sample selection criteria (Fig. 10 and the top panels of Fig. 12). Our quantitative analysis of the Na_I feature shows that this similarity is not necessarily inconsistent with the IMF varying from Chabrier to Salpeter with σ_e. However, this would require yet another conspiracy.

In summary, this study used a subset of the most accurate dynamical models based on MaNGA IFU data and a consistent analysis of IMF-sensitive spectral features for the same galaxies. However, the main finding about the IMF is the absence of clear evidence for the agreement between the two IMF indicators. This implies possible problems with either or both of them.

ACKNOWLEDGEMENTS

We acknowledge the anonymous referee for valuable comments which improved the paper. We also acknowledge Dr Zhiqiang Yan for helpful discussions on the metallicity-dependence of the high-mass-end slope of the initial mass function (IMF). This work is partly supported by the National Key Research and Development Program of China (No. 2018YFA0404501 to SM), by the National Natural Science Foundation of China (Grant Nos. 11821303, 11761131004, and 11761141012). This project is also partly supported by Tsinghua University Initiative Scientific Research Program ID 2019Z07L02017. We also acknowledge the science research grants from the China Manned Space Project with No. CMS-CSST-2021-A11. KZ and RL acknowledge the support of National Natural Science Foundation of China (Nos. 11988101, 11773032, 12022306), the support from the Ministry of Science and Technology of China (No. 2020SKA0110100), the science research grants from the China Manned Space Project (Nos. CMS-CSST-2021-B01, CMS-CSST-2021-A01), CAS Project for Young Scientists in Basic Research (No. YSBR-062), and the support from K.C. Wong Education Foundation.

Funding for the Sloan Digital Sky Survey IV has been provided by the Alfred P. Sloan Foundation, the U.S. Department of Energy Office of Science, and the Participating Institutions.

SDSS-IV acknowledges support and resources from the Centre for High Performance Computing at the University of Utah. The SDSS website is www.sdss.org.

SDSS-IV is managed by the Astrophysical Research Consortium for the Participating Institutions of the SDSS Collaboration including the Brazilian Participation Group, the Carnegie Institution for Science, Carnegie Mellon University, Centre for Astrophysics| Harvard & Smithsonian, the Chilean Participation Group, the French Participation Group, Instituto de Astrofísica de Canarias, The Johns Hopkins University, Kavli Institute for the Physics and Mathematics of the Universe (IPMU) University of Tokyo, the Korean Participation Group, Lawrence Berkeley National Laboratory, Leibniz Institut für Astrophysik Potsdam (AIP), Max-Planck-Institut für Astronomie (MPIA Heidelberg), Max-Planck-Institut für Astrophysik (MPA Garching), Max-Planck-Institut für Extraterrestrische Physik (MPE), National Astronomical Observatories of China, New Mexico State University, New York University, University of Notre Dame, Observatário Nacional/MCTI, The Ohio State University, Pennsylvania State University, Shanghai Astronomical Observatory, United Kingdom Participation Group, Universidad Nacional Autónoma de México, University of Arizona, University of Colorado Boulder, University of Oxford, University of Portsmouth, University of Utah, University of Virginia, University of Washington, University of Wisconsin, Vanderbilt University, and Yale University.

DATA AVAILABILITY

The dynamical and structural properties of MaNGA galaxies used in this work are from the first paper of our MaNGA DynPop series (Zhu et al. 2023). The stellar population properties of these galaxies are from the second paper of this series (Lu et al. 2023). The readers can obtain all these data from the website of MaNGA DynPop (https://manga-dynpop.github.io). The catalogue from the PL JAM model is new from this paper and were included as supplementary material and also included to the DynPop catalogue.

REFERENCES

Abdurro'uf et al., 2022, ApJS, 259, 35
Auger M. W., Treu T., Gavazzi R., Bolton A. S., Koopmans L. V. E., Marshall P. J., 2010, ApJ, 721, L163
Babul A., Rees M. J., 1992, MNRAS, 255, 346
Barber C., Crain R. A., Schaye J., 2018, MNRAS, 479, 5448
Barber C., Schaye J., Crain R. A., 2019a, MNRAS, 482, 2515
Barber C., Schaye J., Crain R. A., 2019b, MNRAS, 483, 985
Bastian N., Covey K. R., Meyer M. R., 2010, ARA&A, 48, 339
Belfiore F. et al., 2019, AJ, 158, 160
Bernardi M., Sheth R. K., Dominguez-Sanchez H., Fischer J. L., Chae K. H., Huertas-Company M., Shankar F., 2018, MNRAS, 477, 2560
Bernardi M., Domínguez Sánchez H., Brownstein J. R., Drory N., Sheth R. K., 2019, MNRAS, 489, 5633
Bernardi M., Sheth R. K., Domínguez Sánchez H., Margalef-Bentabol B., Bizyaev D., Lane R. R., 2023, MNRAS, 518, 3494
Blanton M. R., Kazin E., Muna D., Weaver B. A., Price-Whelan A., 2011, AJ, 142, 31
Bonatto C., Bica E., 2007, MNRAS, 377, 1301
Bryant J. J. et al., 2015, MNRAS, 447, 2857
Bundy K. et al., 2015, ApJ, 798, 7
Cappellari M., 2002, MNRAS, 333, 400
Cappellari M., 2008, MNRAS, 390, 71
Cappellari M., 2016, ARA&A, 54, 597
Cappellari M., 2017, MNRAS, 466, 798
Cappellari M., 2020, MNRAS, 494, 4819
Cappellari M., 2023, MNRAS, 526, 3273
Cappellari M., Emsellem E., 2004, Publ. Astron. Soc. Pac., 116, 138
Cappellari M. et al., 2006, MNRAS, 366, 1126
Cappellari M. et al., 2011, MNRAS, 413, 813
Cappellari M. et al., 2012, Nature, 484, 485
Cappellari M. et al., 2013a, MNRAS, 432, 1709
Cappellari M. et al., 2013b, MNRAS, 432, 1862
Carraro G., Baume G., Piotto G., Méndez R. A., Schmidtobreick L., 2005, A&A, 436, 527
Carter D., Visvanathan N., Pickles A. J., 1986, ApJ, 311, 637

Cenarro A. J., Gorgas J., Vazdekis A., Cardiel N., Peletier R. F., 2003, MNRAS, 339, L12
Chabrier G., 2003, Publ. Astron. Soc. Pac., 115, 763
Choi J., Dotter A., Conroy C., Cantiello M., Paxton B., Johnson B. D., 2016, ApJ, 823, 102
Cid Fernandes R., Mateus A., Sodré L., Stasińska G., Gomes J. M., 2005, MNRAS, 358, 363
Cleveland W. S., Devlin S. J., 1988, J. Am. Stat. Assoc., 83, 596
Conroy C., Gunn J. E., 2010, ApJ, 712, 833
Conroy C., van Dokkum P. G., 2012, ApJ, 760, 71
Conroy C., Gunn J. E., White M., 2009, ApJ, 699, 486
Dekel A., Woo J., 2003, MNRAS, 344, 1131
den Brok M., Krajnović D., Emsellem E., Mercier W., Steinmetz M., Weilbacher P. M., 2024, MNRAS, 530, 3278
Domínguez Sánchez H., Bernardi M., Brownstein J. R., Drory N., Sheth R. K., 2019, MNRAS, 489, 5612
Domínguez Sánchez H., Margalef B., Bernardi M., Huertas-Company M., 2022, MNRAS, 509, 4024
Drory N. et al., 2015, AJ, 149, 77
Dutton A. A. et al., 2013, MNRAS, 428, 3183
Eftekhari F. S. et al., 2022, MNRAS, 517, 4714
Faber S. M., French H. B., 1980, ApJ, 235, 405
Ferreras I., La Barbera F., de La Rosa I. G., Vazdekis A., de Carvalho R. R., Falcon-Barroso J., Ricciardelli E., 2013, MNRAS, 429, L15
Ge J., Mao S., Lu Y., Cappellari M., Long R. J., Yan R., 2021, MNRAS, 507, 2488
Gu M., Greene J. E., Newman A. B., Kreisch C., Quenneville M. E., Ma C.-P., Blakeslee J. P., 2022, ApJ, 932, 103
Jeong H., Yi S. K., Kyeong J., Sarzi M., Sung E.-C., Oh K., 2013, ApJS, 208, 7
Kroupa P., 2001, MNRAS, 322, 231
Kroupa P., Tout C. A., Gilmore G., 1993, MNRAS, 262, 545
Kuntschner H., 2004, A&A, 426, 737
La Barbera F., de Carvalho R. R., de La Rosa I. G., Lopes P. A. A., Kohl-Moreira J. L., Capelato H. V., 2010, MNRAS, 408, 1313
La Barbera F., Ferreras I., Vazdekis A., de la Rosa I. G., de Carvalho R. R., Trevisan M., Falcón-Barroso J., Ricciardelli E., 2013, MNRAS, 433, 3017
La Barbera F., Ferreras I., Vazdekis A., 2015, MNRAS, 449, L137
La Barbera F. et al., 2019, MNRAS, 489, 4090
Lablanche P.-Y. et al., 2012, MNRAS, 424, 1495
Lacerda E. A. D. et al., 2022, New A, 97, 101895
Law D. R. et al., 2015, AJ, 150, 19
Law D. R. et al., 2016, AJ, 152, 83
Li H., Li R., Mao S., Xu D., Long R. J., Emsellem E., 2016, MNRAS, 455, 3680
Li H. et al., 2017, ApJ, 838, 77
Li H. et al., 2018, MNRAS, 476, 1765
Li J., Liu C., Zhang Z.-Y., Tian H., Fu X., Li J., Yan Z.-Q., 2023, Nature, 613, 460
Li S., Li R., Zhu K., Lu S., Cappellari M., Mao S., Wang C., Gao L., 2024, MNRAS, 529, 4633
Loubser S. I., Hoekstra H., Babul A., Bahé Y. M., Donahue M., 2021, MNRAS, 500, 4153
Lu S., Zhu K., Cappellari M., Li R., Mao S., Xu D., 2023, MNRAS, 526, 1022
Lyubenova M. et al., 2016, MNRAS, 463, 3220
McConnell N. J., Ma C.-P., Gebhardt K., Wright S. A., Murphy J. D., Lauer T. R., Graham J. R., Richstone D. O., 2011, Nature, 480, 215
Marks M., Kroupa P., Dabringhausen J., Pawlowski M. S., 2012, MNRAS, 422, 2246
Marsden C., Shankar F., Bernardi M., Sheth R. K., Fu H., Lapi A., 2022, MNRAS, 510, 5639
Martin C. L., 1999, ApJ, 513, 156
Martín-Navarro I., La Barbera F., Vazdekis A., Falcón-Barroso J., Ferreras I., 2015a, MNRAS, 447, 1033
Martín-Navarro I. et al., 2015b, ApJ, 806, L31
McDermid R. M. et al., 2014, ApJ, 792, L37
Mehrgan K., Thomas J., Saglia R., Parikh T., Neureiter B., Erwin P., Bender R., 2024, ApJ, 961, 127
Mitzkus M., Cappellari M., Walcher C. J., 2017, MNRAS, 464, 4789
Moraux E., Bouvier J., Stauffer J. R., Cuillandre J. C., 2003, A&A, 400, 891
Navarro J. F., Frenk C. S., White S. D. M., 1997, ApJ, 490, 493
Parikh T. et al., 2018, MNRAS, 477, 3954
Phelps R. L., Janes K. A., 1993, AJ, 106, 1870
Poci A., Cappellari M., McDermid R. M., 2017, MNRAS, 467, 1397
Reid I. N., Gizis J. E., 1997, AJ, 113, 2246
Rousseeuw P., Driessen K., 2006, Data Min. Knowl. Discov., 12, 29
Saglia R. P., Maraston C., Thomas D., Bender R., Colless M., 2002, ApJ, 579, L13
Salpeter E. E., 1955, ApJ, 121, 161
Sánchez S. F. et al., 2016a, Rev. Mex. Astron. Astrofis., 52, 21
Sánchez S. F. et al., 2016b, Rev. Mex. Astron. Astrofis., 52, 171
Santucci G. et al., 2022, ApJ, 930, 153
Schaye J. et al., 2015, MNRAS, 446, 521
Schwarzschild M., 1979, ApJ, 232, 236
Shetty S., Cappellari M., McDermid R. M., Krajnović D., de Zeeuw P. T., Davies R. L., Kobayashi C., 2020, MNRAS, 494, 5619
Smee S. A. et al., 2013, AJ, 146, 32
Smith R. J., 2014, MNRAS, 443, L69
Smith R. J., 2020, ARA&A, 58, 577
Spiniello C., Trager S. C., Koopmans L. V. E., Chen Y. P., 2012, ApJ, 753, L32
Spiniello C., Trager S. C., Koopmans L. V. E., 2015, ApJ, 803, 87
Stoughton C. et al., 2002, AJ, 123, 485
Thomas J. et al., 2011, MNRAS, 415, 545
Toloba E. et al., 2014, ApJS, 215, 17
Tortora C., La Barbera F., Napolitano N. R., 2016, MNRAS, 455, 308
Trager S. C., Worthey G., Faber S. M., Burstein D., González J. J., 1998, ApJS, 116, 1
Treu T., Auger M. W., Koopmans L. V. E., Gavazzi R., Marshall P. J., Bolton A. S., 2010, ApJ, 709, 1195
van Dokkum P. G., Conroy C., 2010, Nature, 468, 940
van Dokkum P. G., Conroy C., 2012, ApJ, 760, 70
van Dokkum P., Conroy C., Villaume A., Brodie J., Romanowsky A. J., 2017, ApJ, 841, 68
Virtanen P. et al., 2020, Nat. Methods, 17, 261
Wake D. A. et al., 2017, AJ, 154, 86
Wang C. et al., 2024, MNRAS, 527, 1580
Westfall K. B. et al., 2019, AJ, 158, 231
Wilkinson D. M., Maraston C., Goddard D., Thomas D., Parikh T., 2017, MNRAS, 472, 4297
Woo J., Walters D., Archinuk F., Faber S. M., Ellison S. L., Teimoorinia H., Iyer K., 2024, MNRAS, in press
Worthey G., Faber S. M., Gonzalez J. J., Burstein D., 1994, ApJS, 94, 687
Wyithe J. S. B., Turner E. L., Spergel D. N., 2001, ApJ, 555, 504
Yan R. et al., 2016a, AJ, 151, 8
Yan R. et al., 2016b, AJ, 152, 197
Yan Z., Jerabkova T., Kroupa P., 2017, A&A, 607, A126
Yan Z., Jerabkova T., Kroupa P., Vazdekis A., 2019, A&A, 629, A93
Yan Z., Jeřábková T., Kroupa P., 2021, A&A, 655, A19
Zhou S. et al., 2019, MNRAS, 485, 5256
Zhu K., Lu S., Cappellari M., Li R., Mao S., Gao L., 2023, MNRAS, 522, 6326
Zhu K., Lu S., Cappellari M., Li R., Mao S., Gao L., Ge J., 2024, MNRAS, 527, 706

This paper has been typeset from a TEX/LATEX file prepared by the author.